ION

Instantaneous Sub-meter Level Precise Point Positioning of Low-Cost Smartphones

Jiale Wang[1] | Fu Zheng*[2] | Yong Hu[1] | Dong Zhang[1] | Chuang Shi[1,2,3]

[1] School of Electronics and Information Engineering, Beihang University Beijing, China

[2] Research Institute for Frontier Science, Beihang University Beijing, China

[3] Key Laboratory of Satellite Navigation and Mobile Communication Fusion Technology, Ministry of Industry and Information Technology Beijing, China

Correspondence
Fu Zheng
Research Institute for Frontier Science
Beihang University, Beijing, China.
Email: fzheng@buaa.edu.cn

Abstract

The prevalence of inexpensive global navigation satellite system (GNSS) chips that facilitate the performance of carrier phase measurements has provided hardware that can be used as the foundation for implementing precise point positioning (PPP) of low-cost smartphones. However, because of the atmospheric delays and high measurement noise associated with low-quality patch antennae, the convergence time of smartphone PPP can increase from minutes to even hours. By establishing the Satellite-based Ionospheric Model (SIM) and Real-time Tropospheric Grid Point (RTGP) models, we aim to achieve instantaneous sub-meter level positioning for smartphone PPP. In both kinematic and static experiments, Xiaomi Mi8 and Huawei P40 smartphone signals can converge to sub-meter accuracy in the horizontal direction within one to six seconds when adopting multi-constellation and dual-frequency PPP solutions augmented by precise atmospheric corrections. The atmospheric augmentation PPP method effectively improves the convergence speed and positioning accuracy compared to what can be achieved using the conventional PPP algorithm, thereby satisfying smartphone users' demand for rapid and high-accuracy positioning.

Keywords

atmospheric augmentation, convergence time, instantaneous sub-meter level positioning, smartphone PPP

1 | INTRODUCTION

With the popularity of smartphones in both studies and mass markets, the demand for low-cost terminals with high-accuracy positioning has expanded significantly. In 2016, Google stated at the Android Developer Conference that the Android N operating system would permit access to raw global navigation satellite system (GNSS) observations. This project marks a turning point for this technology, as early smartphones had only limited ability to access high-quality GNSS observations (Li & Geng, 2019). In 2018, Xiaomi launched the Xiaomi Mi8, the world's first dual-frequency GNSS smartphone with the Broadcom BCM 47755 processor that incorporated GPS/QZSS L5 signals and the Galileo E5a signal

(Paziewski et al., 2019; Robustelli et al., 2021). Since then, prominent chipmakers, including Qualcomm, Broadcom, and Haise have introduced processors that support multi-constellation and dual-frequency GNSS measurements, all of which support smartphone high-precision positioning capabilities.

Since the release of Android 7.0, numerous data processing methods and filtering techniques have been proposed to reduce the influence of linearly-polarized microstrip antenna error on smartphone positioning. Specifically, several researchers have used a carrier-to-noise ratio-based stochastic model in weighting strategies designed to mitigate the impact of multipath. This is because the carrier-to-noise ratio can better reflect the GNSS measurement quality of smartphones than elevation (F. Liu et al., 2021; L. Wang et al., 2021; Yi et al., 2021). In the data preprocessing stage, strict data quality control approaches such as multipath suppression based on wavelet transform, Doppler-smoothing pseudorange, and three-dimensional (3D)-mapping–aided GNSS were implemented (Adjrad et al., 2019; W. Li et al., 2021; Ng et al., 2021; Zhang et al., 2019). Several filtering strategies, including the time-differenced filtering approach, Hatch filtering, and factor graph optimization have been presented to manage the complex smartphone usage environment (Geng et al., 2019; Guo et al., 2020; Zhang et al., 2018).

Implementation of the aforementioned methods has considerably improved the positioning accuracy of smartphones, with some studies achieving decimeter or centimeter-level positioning accuracy using low-cost Android devices. For example, researchers at GEO++ employed an absolute antenna field robot to estimate the antenna phase center of a Huawei mate20X smartphone (Darugna et al., 2020) and achieved a reliable real-time kinematic (RTK) fix solution in less than three minutes by calibrating the antenna phase center. Several other researchers also described the use of RTK to realize the centimeter-level positioning of smartphones (Geng & Li, 2019; Paziewski et al., 2021; Wanninger & Heßelbarth, 2020; Yong et al., 2021; Zeng et al., 2022). Although this method facilitates the rapid acquisition of high-accuracy positioning information, one of the main drawbacks of RTK includes its reliance on reference stations with communication links. Furthermore, atmospheric delays will have a significant impact on positioning performance as baseline distance increases (Dabove & Di Pietra, 2019; Darugna et al., 2019; Magalhães et al., 2021; Yuan et al., 2022).

Consequently, an increasing number of studies have concentrated on PPP technology, in which a single smartphone is used to calculate precise positioning without the need for external reference stations. Wu et al. (2019) evaluated the dual-frequency GPS L1/L5 and GALILEO E1/E5a observations of the Xiaomi Mi8 smartphone using the ionosphere-free PPP (IF-PPP) model and reported that it took 102 minutes for the horizontal positioning accuracy to converge to 1 m. M. Li et al. (2021) assessed the positioning accuracy of a Huawei P40 smartphone in static single-frequency PPP mode, with the east, north, and up directions converging to 0.72, 0.51, and 0.66, respectively after 30 minutes. Wang et al. (2020) and Q. Liu et al. (2021) adopted a global ionospheric grid model and a regional precision ionospheric model as constraints to improve the convergence speed of smartphone PPP. They demonstrated that it is possible to reduce the long convergence time to a few minutes using precise ionospheric corrections.

Despite significant progress, the main limitations of smartphone PPP are unstable positioning performance and long convergence times ranging from a few minutes to several hours. Even in the open static environment, the convergence time to 1 m in the horizontal direction still takes several minutes. This time delay cannot meet smartphone users' demand for instantaneous

sub-meter-level positioning. In addition, previous studies primarily evaluated the influence of ionospheric correction on convergence without considering the constraint of precise tropospheric correction. To achieve rapid and reliable smartphone navigation, we will utilize the high-precision ionospheric and tropospheric corrections as *a priori* constraint information and will further explore the potential of multi-constellation and dual-frequency PPP for Android smartphones.

The remainder of this paper is structured as follows. We derived a mathematical model of atmospheric augmentation PPP in Section 2 from the basic observation equation of undifferenced and uncombined PPP and the virtual observation equations of atmospheric corrections. Section 3 presents the experimental data set, quality assessment, and data processing strategies. The experimental results and analysis are presented in Section 4. Finally, conclusions and future work are considered in Section 5.

2 | METHODOLOGY

In this section, we combine the basic observation equations of undifferenced and uncombined PPP with the virtual equations of the ionosphere and troposphere corrections to generate a functional model of atmospheric augmentation PPP. We also describe ionospheric and tropospheric variance information and a carrier-to-noise ratio-dependent stochastic model for smartphones with polarized microstrip antennae. According to the RINEX 3.05 specification, the GPS, GLONASS, BDS, Galileo, and QZSS are denoted by the letters G, R, C, E, and J, respectively. At the same time, the symbols used to denote other variables were consistently abbreviated to their corresponding English letters.

2.1 | Undifferenced and Uncombined PPP Model

The undifferenced and uncombined PPP model of pseudorange and carrier phase is shown in Equation (1) (Gong et al., 2022; Li et al., 2018):

$$
\begin{cases}
P_{r,f}^s = \rho_r^s + c\left(t_r - t^s\right) + a_r^s T_{r,z} + \dfrac{40.3}{f^2}\gamma_r^s I_r^s + c\left(b_{r,f} - b_f^s\right) + \varepsilon_P \\[2mm]
\Phi_{r,f}^s = \rho_r^s + c\left(t_r - t^s\right) + a_r^s T_{r,z} - \dfrac{40.3}{f^2}\gamma_r^s I_r^s + \lambda_f\left(N_{r,f}^s + B_{r,f} - B_f^s\right) + \varepsilon_\Phi
\end{cases}
\tag{1}
$$

where $r, f,$ and s refer to the receiver, frequency, and satellite, respectively; ρ_r^s is the geometric distance from the receiver to the satellite; t_r and t^s denote the receiver and satellite clock error in seconds, respectively; $b_{r,f}$ and b_f^s represent the receiver-related and satellite-related pseudorange hardware delay in seconds, respectively; $B_{r,f}$ and B_f^s represent the receiver-related and satellite-related phase hardware delay in cycles, respectively; $T_{r,z}$ and a_r^s are the tropospheric zenith delay (ZTD) and mapping function, respectively; $I_{r,f}^s$ and γ_r^s indicate the zenith total electron content and mapping function, respectively; λ_f and $N_{r,f}^s$ represent the wavelength and integer ambiguity in cycles, respectively; and ε_P and ε_Φ are the hardware noise, multipath, and unmodeled error for pseudorange and carrier phase, respectively.

Equation (1) accounts for the primary source of GNSS signal propagation path error. The remaining errors, such as ocean tide loading, solid earth tide, relativistic

effect, the Earth's rotation, antenna phase center correction, and phase windup can be corrected by the corresponding models. The phase hardware delays were not estimated because the float ambiguity solution of PPP is used in this analysis. After compensating for the satellite-related pseudorange hardware delay and the prior tropospheric delay, the linearized error equation of Equation (1) can be expressed as shown in Equation (2):

$$
\begin{cases}
\Delta P_{r,f}^s = u_r^s \Delta x_r + ct_r + a_r^s T_w + \dfrac{40.3}{f^2}\gamma_r^s I_r^s + cb_{r,f} + \varepsilon_P \\[2mm]
\Delta \Phi_{r,f}^s = u_r^s \Delta x_r + ct_r + a_r^s T_w - \dfrac{40.3}{f^2}\gamma_r^s I_r^s + \lambda_f N_{r,f}^s + \varepsilon_\Phi
\end{cases}
\tag{2}
$$

where $\Delta P_{r,f}^s$ and $\Delta \Phi_{r,f}^s$ represent the observed-minus-calculated (OMC) of the pseudorange and carrier phase, respectively; u_r^s and Δx_r indicate the unit vector from satellite to the receiver and the receiver position increments relative to the prior position, respectively; and T_w denotes the residual of zenith tropospheric wet delay.

2.2 | Atmospheric Augmentation PPP Model

Considering the ionospheric delay and residual tropospheric wet delay as shown in Equation (2), we then introduced the virtual atmospheric observation equations (Zheng et al., 2019; Zheng et al., 2018) as shown in Equation (3):

$$
\begin{cases}
\tilde{I}_r^s = a_0 + a_1 dL + a_2 dB + a_3 dL^2 + a_4 dB^2 + r_r^s + \varepsilon_{\tilde{I}_r^s} \\[2mm]
\tilde{T} = T_w + \varepsilon_{\tilde{T}}
\end{cases}
\tag{3}
$$

where $\tilde{I}_r^s$ is the virtual observable of vertical ionospheric delay derived from the Global Ionospheric Map (GIM) or other available ionospheric models; a_0 represents the average of the ionospheric delay over the station; $a_i (i = 1,2,3,4)$ denotes the coefficient of two second-order polynomials used to fit the horizontal gradients of east-west and south-north directions, respectively; dL and dB are the differences in latitude and longitude between the ionospheric pierce point (IPP) and the approximate position of the station, respectively; r_r^s is the residual of ionospheric effect that describes the stochastic behavior of ionospheric delay for each satellite; $\varepsilon_{\tilde{I}_r^s}$ is the noise of the ionospheric model correction; $\tilde{T}$ indicates the virtual observation of the tropospheric wet delay calculated from empirical or other models developed by using ground-based GNSS observations; and $\varepsilon_{\tilde{T}}$ is the noise of the tropospheric model correction.

Combining the basic PPP Equation (2) with the virtual Equation (3) of the ionosphere and troposphere, the observation equation of atmospheric augmentation PPP can be obtained as shown in Equation (4):

$$
\begin{cases}
\Delta P_{r,f}^s = u_r^s \Delta x_r + ct_r + a_r^s T_w + \dfrac{40.3}{f^2}\gamma_r^s \cdot \left(a_0 + a_1 dL + a_2 dB + a_3 dL^2 + a_4 dB^2 + r_r^s\right) + cb_{r,f} + \varepsilon_P \\[2mm]
\Delta \Phi_{r,f}^s = u_r^s \Delta x_r + ct_r + a_r^s T_w - \dfrac{40.3}{f^2}\gamma_r^s \cdot \left(a_0 + a_1 dL + a_2 dB + a_3 dL^2 + a_4 dB^2 + r_r^s\right) + \lambda_f N_{r,f}^s + \varepsilon_\Phi \\[2mm]
\tilde{I}_r^s = a_0 + a_1 dL + a_2 dB + a_3 dL^2 + a_4 dB^2 + r_r^s + \varepsilon_{\tilde{I}_r^s} \\[2mm]
\tilde{T} = T_w + \varepsilon_{\tilde{T}}
\end{cases}
\tag{4}
$$

Assuming that a dual-frequency receiver r tracked j satellites for a given epoch, the GNSS observation model in matrix form can be expressed as shown in Equation (5):

$$l = Bx + v \tag{5}$$

where l, B, and x are the observation vector, the design matrix, and the parameter vector to be estimated, respectively. Their specific forms are shown in Equation (6):

$$\begin{cases} l = \begin{pmatrix} \Delta P_{r,1} & \Delta P_{r,5} & \Delta \Phi_{r,1} & \Delta \Phi_{r,5} & \tilde{I}_r^s & \tilde{T} \end{pmatrix}^T \\ x = \begin{pmatrix} \Delta x_r & t_r & b_r & N_r & a_r & r_r & T_w \end{pmatrix}^T \\ B = \begin{pmatrix} B_{\Delta x_r} & B_{t_r} & B_{b_{r,f}} & B_{N_r} & B_{a_r} & B_{r_r} & B_{T_w} \end{pmatrix}^T \end{cases} \tag{6}$$

where $\Delta P_{r,f} = \begin{pmatrix} \Delta P_{r,f}^1 & \cdots & \Delta P_{r,f}^j \end{pmatrix}^T$ and $\Delta \Phi_{r,f} = \begin{pmatrix} \Delta \Phi_{r,f}^1 & \cdots & \Delta \Phi_{r,f}^j \end{pmatrix}^T$ are the OMC of pseudorange and carrier phase observations at different frequencies $f \in \begin{pmatrix} 1 & 5 \end{pmatrix}$; t_r represents the receiver clock error for different GNSS systems; $\tilde{I}_r^s = \begin{pmatrix} \tilde{I}_r^1 & \cdots & \tilde{I}_r^j \end{pmatrix}^T$ denotes the virtual observation vectors of vertical ionospheric delay derived from the *a priori* ionospheric model; $N_r = \begin{pmatrix} N_{r,1}^1 & \cdots & N_{r,1}^j, & N_{r,5}^1 & \cdots & N_{r,5}^j \end{pmatrix}^T$ is the ambiguity vector on both frequencies; $r_r = \begin{pmatrix} r_r^1 & \cdots & r_r^j \end{pmatrix}^T$, and $a_r = \begin{pmatrix} a_0 & a_1 & a_2 & a_3 & a_4 \end{pmatrix}^T$ are the vectors of stochastic and deterministic ionospheric parameters, respectively. Each vector in the design matrix B corresponds to the estimated coefficient matrix of the parameter.

2.3 | Stochastic Model

The stochastic model plays a well-known and crucial role in the process of generating high-precision GNSS data. The positioning accuracy will be significantly affected if the variance information cannot accurately describe the observation error. Assuming that pseudorange, carrier phase, and virtual observations of the ionosphere and troposphere are independent of one another, we can obtain the variance matrix D of the stochastic model of atmospheric augmentation PPP strategy as shown in Equation (7):

$$D \begin{Bmatrix} P \\ \phi \\ \tilde{I} \\ \tilde{T} \end{Bmatrix} = \begin{bmatrix} \sigma_P^2 & 0 & 0 & 0 \\ 0 & \sigma_\phi^2 & 0 & 0 \\ 0 & 0 & \sigma_{\tilde{I}}^2 & 0 \\ 0 & 0 & 0 & \sigma_{\tilde{T}}^2 \end{bmatrix} \tag{7}$$

where σ_P^2 and σ_ϕ^2 represent the GNSS observation variances of pseudorange and carrier phase, respectively; and $\sigma_{\tilde{I}}^2$ and $\sigma_{\tilde{T}}^2$ denote the prior variances corresponding to the ionospheric and tropospheric virtual observations, respectively.

2.3.1 | GNSS Observation Variances

In general, an elevation-dependent weighting model is usually used to process the observations of the survey-grade or geodetic receivers in GNSS applications. The standard deviation of code noise (σ_{P_0}) and phase noise (σ_{L_0}) with satellite

elevation (*el*) are then used to derive the prior standard deviation as denoted in Equation (8) (Shinghal & Bisnath, 2021):

$$\begin{cases} \sigma_P^s = \sqrt{\sigma_{P_0}^2 / \sin^2\left(el^s\right)} \\ \sigma_\phi^s = \sqrt{\sigma_{\phi_0}^2 / \sin^2\left(el^s\right)} \end{cases} \tag{8}$$

where σ_P^s and σ_ϕ^s are the prior weights corresponding to each satellite s and the elevation *el*, respectively. Generally, σ_{P_0} ranges from 0.02 to 0.03 m and σ_{L_0} ranges from 0.002 to 0.003 m for geodetic receivers. Unfortunately, smartphones and other mobile devices are typically equipped with low-gain microstrip linearly polarized antennae to minimize size and cost. Because linearly polarized antennae are highly sensitive to signals from all directions (including multipath error) the quality of smartphone GNSS data is severely degraded. Numerous buildings and trees found in complex environments would block GNSS signals even further, resulting in severe code noise and multipath error in GNSS measurement data.

Previous studies have demonstrated that the quality of GNSS observation data from smartphones is strongly correlated with the carrier-to-noise ratio and has almost no relationship with elevation (Gao et al., 2021; Liu et al., 2019). Given that the carrier-to-noise ratio is one of the most important indications for determining the quality of GNSS measurements, this parameter might be used as an effective alternative for stochastic modeling. In this case, we obtained a weighting model for GNSS observations of smartphones with respect to the improvement of the classical carrier-to-noise ratio stochastic model as shown in Equation (9) (Brunner et al., 1999; Wieser & Brunner, 2000):

$$\begin{cases} \sigma^s_{P_f} = \sigma_{P_0} \sqrt{V_f + C_f * 10^{-\frac{C/N_0}{10}}} \\ \sigma^s_{\phi_f} = \sigma_{\phi_0} \sqrt{V_f + C_f * 10^{-\frac{C/N_0}{10}}} \end{cases} \tag{9}$$

where $\sigma^s_{P_f}$ and $\sigma^s_{\phi_f}$ are the standard deviation of the measurement error determined by the C/N_0 value. Because the accuracy of the GNSS observations varies significantly among various satellite systems and frequencies of smartphones, parameters V_f and C_f need to be calibrated according to satellite systems $s \in \begin{pmatrix} G & R & C & E & J \end{pmatrix}$ and signal frequencies $f \in \begin{pmatrix} 1 & 5 \end{pmatrix}$ rather than set to the same value. We recommend adopting the short baseline single-differenced method proposed by Zhang et al. (2018) to calibrate these coefficients, as this can fully describe the relationship between the GNSS measurement error and the carrier-to-noise ratio for each device.

2.3.2 | *Atmospheric Observation Variances*

In addition to the conventional GPT2w and GIM models which were used to characterize the contributions of precise atmospheric corrections on rapid high-precision positioning for smartphone PPP, we also utilized the precise ionospheric and tropospheric models known as the Satellite-based Ionospheric Model (SIM) and Real-time Tropospheric Grid Point (RTGP), respectively. More detailed information on the SIM and the RTGP can be found in previous publications (Zheng et al., 2019; Zheng et al., 2018). When different atmospheric corrections are used in the augmented PPP model, the variance of ionospheric and tropospheric

virtual observations will depend on the precision of the external correction model. Different atmospheric delay correction models will need to set alternative weights to generate a precise description of the model's accuracy. PPP processing can be satisfied with varying atmospheric corrections by adjusting the values of σ_I and σ_T, even in the absence of inputs from external atmospheric products.

The results of validations of precise atmospheric corrections will be presented in Section 3.2. Variance information for the different tropospheric and ionospheric models will then be determined.

3 | EXPERIMENT AND ANALYSIS

To evaluate the positioning performance of atmospheric augmentation PPP, we conducted static and kinematic experiments in Beijing and collected GNSS observation data from various Android smartphones. Simultaneously, we also obtained observation data from 28 reference stations surrounding the experimental location to generate precise atmospheric corrections and assess the quality of the atmospheric products. We then propose effective methods to improve the data quality based on the characteristics of the smartphones' GNSS observations and present a flow chart of the atmospheric augmentation PPP algorithm and a processing strategy table.

3.1 | GNSS Data Collection

The static experiment was conducted from 05:30 to 06:00 on March 7, 2021 (UTC), as shown in Figure 1. Several smartphones were placed in an open-sky square during the experiment. A Geo++ RINEX Logger was used to record multi-GNSS observation data. Meanwhile, a Septentrio receiver was deployed several meters away for comparison. The reference position of each smartphone was calibrated with a handheld RTK receiver made by Stonex. When connecting to the Network RTK server, the Stonex S3II receiver can output a coordinate better than 1 cm within a few seconds which can be used as the reference position. Notably, because the smartphone antenna phase center is unknown, the reference position is uniformly assigned as the geometric center of each device.
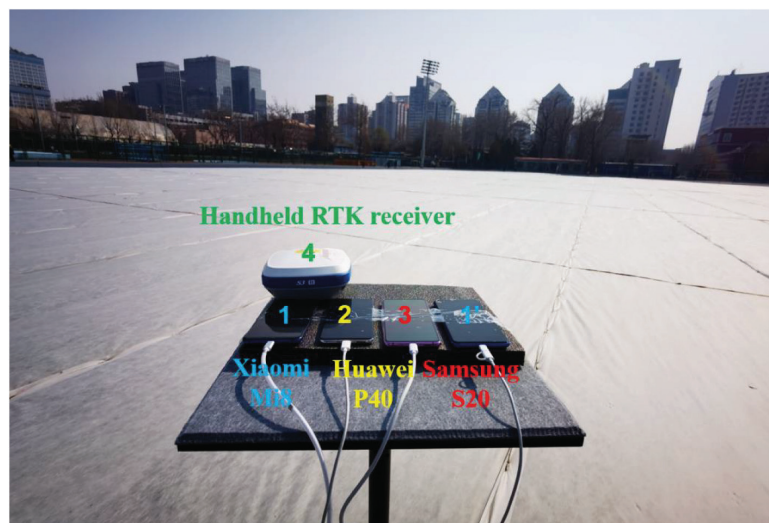

FIGURE 1 Static scenario and experimental devices used in the test

FIGURE 2 Overhead view of the kinematic experiment with associated illustrations and annotations
The red curve represents the experimental trajectory. The image on the left shows the experimental scene; the image on the right depicts a base station that was 0.45 km from the experimental location.

Shown are (1) Xiaomi MI8, (2) Huawei P40, (3) Samsung S20, and (4) a handheld RTK receiver for calibrating the reference position.

The kinematic experiment was conducted between 03:16 and 03:26, March 14, 2021 (UTC). As depicted in Figure 2, several smartphones and a Septentrio mosaic-X5 receiver were placed on a laboratory trolley that was moved forward by the experimenter. The reference device uses a Septentrio receiver equipped with the mosaic-X5 module, which supports multi-constellation, multi-frequency, and all-in-view satellite tracking. Because the base station and Septentrio mosaic-X5 receiver form a short baseline (less than 1 km), we can obtain a kinematic centimeter-level reference trajectory by Post-Processed Kinematic (PPK). The error between each smartphone's geometric center and the center of the Septentrio antenna has been compensated by lever arm correction.

In this experiment, the primary purpose of the Septentrio receiver was to compare the characteristics of smartphone observations and provide an accurate reference trajectory. Moreover, because the GNSS chipset on the Samsung S20 does not support carrier phase measurements, our experiments exclusively evaluate the PPP performance of the Xiaomi Mi8, Huawei P40, and Septentrio mosaic-x5. Table 1 summarizes the characteristics of the experimental devices and their GNSS support capabilities.

3.2 | Atmospheric Quality Assessments

To extract precise atmospheric corrections, we selected 28 reference stations surrounding the experimental location, including 27 stations for atmospheric modeling and one station for the assessment of atmospheric quality. Figure 3 depicts the distribution of the experimental location and reference stations selected for this experiment. The red star denotes the location of kinematic and static experiments in Beijing and the blue dots represent the stations used for atmospheric modeling. We included one unmodeled station (magenta dot) to assess the quality of atmospheric models.

TABLE 1
Experimental Devices and Their Ability to Support Each GNSS Constellation and Frequency

Constellation and frequency		Septentrio mosaic-x5		Xiaomi Mi8		Huawei P40		Samsung S20	
		Code	Phase	Code	Phase	Code	Phase	Code	Phase
GPS	L1	√	√	√	√	√	√	√	×
	L5	√	√	√	√	√	√	×	×
GLONASS	G1	√	√	√	√	√	√	√	×
BDS-2	B1I	√	√	√	√	√	√	√	×
BDS-3	B1I	√	√	√	√	√	√	√	×
Galileo	E1	√	√	√	√	√	√	√	×
	E5a	√	√	√	√	√	√	×	×
QZSS	L1	√	√	√	√	√	√	√	×
	L5	√	√	√	√	√	√	×	×

Note: GPS: Global Positioning System; GLONASS: Global Navigation Satellite System; BDS-2: BeiDou-2 Navigation Satellite System; BDS-3: BeiDou-3 Navigation Satellite System; Galileo: European Global Navigation Satellite System; QZSS: Quasi-Zenith Satellite System.
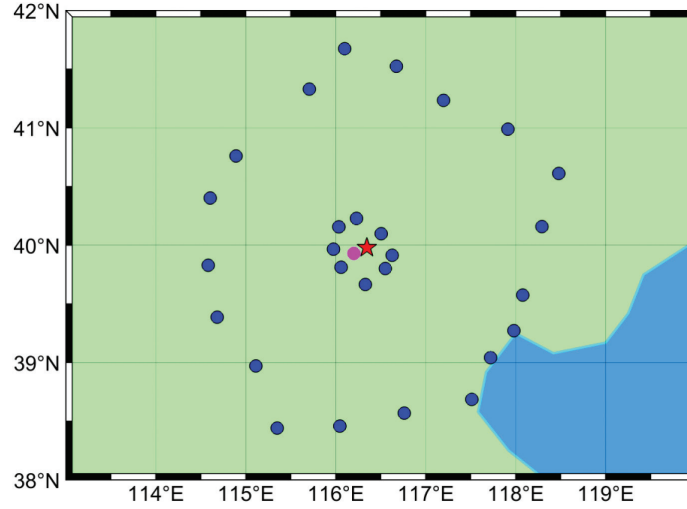
FIGURE 3 Location of the kinematic and static experiments in Beijing (red star), the unmodeled station (magenta dot), and the distribution of stations used for atmospheric modeling (blue dots)

Undifferenced and uncombined PPP technology is a high-precision data processing method that can make full use of the raw GNSS observations and accurately retrieve ionospheric slant TEC (STEC) and zenith tropospheric delay (ZTD) data. Therefore, PPP-derived STEC (Liu et al., 2018; Z. Wang et al., 2021) and PPP-derived ZTD (Gratton et al., 2021; Zhao et al., 2018) are proposed as effective reference values to evaluate the accuracy of ionospheric and tropospheric models.

The formula for assessing the accuracy of ionospheric and tropospheric models using RMS is shown in Equation (10):

$$\begin{cases} RMS_I = RMS\{STEC_I - STEC_{PPP}\} = \sqrt{\dfrac{\sum\limits_{i=1}^{n}\left(STEC_{I,i} - STEC_{PPP,i}\right)^2}{n-1}} \\ RMS_T = RMS\{ZTD_T - ZTD_{PPP}\} = \sqrt{\dfrac{\sum\limits_{i=1}^{n}\left(ZTD_{T,i} - ZTD_{PPP,i}\right)^2}{n-1}} \end{cases} \tag{10}$$

where n is the total number of epochs; RMS_I and RMS_T denote the root mean square error (RMS) of the ionospheric and tropospheric models, respectively; $STEC_{I,i}$ and $STEC_{PPP,i}$ denote the slant TEC estimated by the GIM/SIM model and PPP at the ith epoch, respectively; $ZTD_{T,i}$ and $ZTD_{PPP,i}$ denote the zenith tropospheric delay estimated by the GPT2w/RTGP model and PPP at the ith epoch, respectively.

We assessed the accuracy of the ionospheric and tropospheric corrections from 03:00 to 08:00 on March 7, 2021 (UTC), using a station that was not involved in the modeling (i.e., the magenta dot shown in Figure 3). To illustrate the effectiveness of the established atmospheric models, we compared CODE's GIM products with SIM and the GPT2w model with the RTGP model. The left panel of Figure 4 presents a comparison of the ionospheric STEC accuracy of the G28 satellite with GIM and SIM, while the right panel shows the ZTD accuracy with GPT2w and RTGP. It should be noted that the RTGP model was only used to enhance the tropospheric wet delay (ZWD); the tropospheric dry delay (ZHD) was still estimated by the GPT2w model. Therefore, the zenith tropospheric delay (ZTD = ZHD + ZWD) evaluated below reflects an improvement in ZWD accuracy.

As shown in Figure 4, the accuracies of our proposed SIM and RTGP models are better than those of the GIM and GPT2w models. The GIM model has an accuracy of approximately 3 TECU, while the GPT2w model has an accuracy of approximately 2.5 cm. We employed the Satellite-based Ionospheric Model (SIM) for ionospheric STEC modeling; the RMS of the model's accuracy is better than 1 TECU. Likewise, the accuracy of the Real-Time Tropospheric Grid Point (RTGP) model is better than 1.2 cm in RMS. Based on the combination of the evaluations of the different atmospheric models featured in this work and detailed quality assessments of the precise atmospheric products performed previously (Zheng et al., 2019; Zheng et al., 2018), the standard deviation σ_T of the tropospheric delay model is equal to 0.04 m when using the GPT2w model; we set this value to 0.01 m when using the RTGP model. The standard deviation σ_I of the ionospheric delay model is equal to 6 TECU when using the GIM model, while we set it to 1 TECU when using the SIM model. Table 2 presents the standard deviations determined for the various tropospheric and ionospheric models.
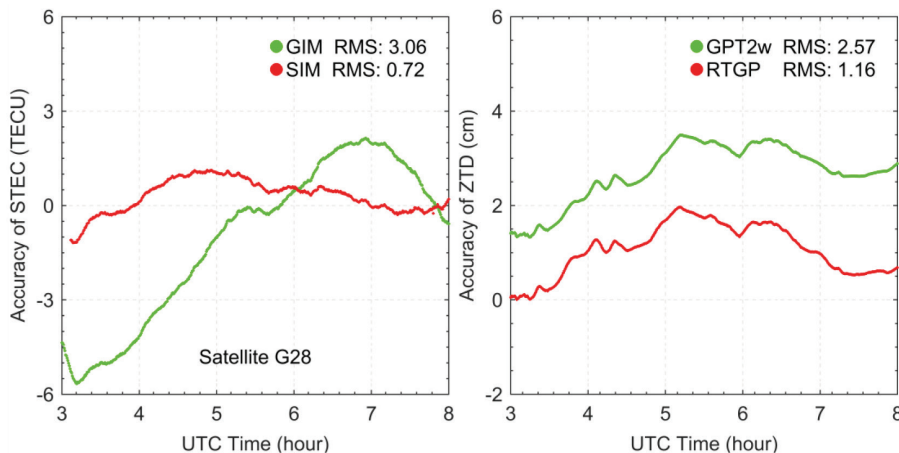

FIGURE 4 Accuracy comparison between the ionospheric and tropospheric models PPP-derived STEC and ZTD are used as reference values for the ionospheric and tropospheric models to calculate the RMS for each model.

3.3 | Processing Strategies

The consumer GNSS chips and microstrip antennae used in low-cost smartphones cause high measurement noise, severe multipath, low signal gain, and frequent cycle slips in the observation data. Therefore, to achieve sub-meter level smartphone positioning, the GNSS data processing algorithms and the precise correction of propagation path error will need to be handled strictly. Figure 5 depicts the overall flowchart of the atmospheric augmentation PPP algorithm based on the mathematical methods proposed above and our previous experience in dealing with GNSS data from smartphones.

Based on the atmospheric augmentation PPP strategy described above, we employed raw GNSS measurements from Android API to generate RINEX 3.04 observations, including the pseudorange, carrier phase, Doppler, and carrier-to-noise ratio. Given the significant measurement error of the pseudorange observations, we applied the Doppler-smoothing pseudorange scheme to reduce

TABLE 2
Standard Deviations for Various Tropospheric and Ionospheric Models.

Atmospheric delays	Model	Standard deviation
Ionospheric delay	GIM	6 TECU
	SIM	1 TECU
Tropospheric delay	GPT2w	0.04 m
	RTGP	0.01 m

Note: GIM: Global Ionospheric Model; SIM: Satellite-based Ionospheric Model;
GPT2w: Global Pressure and Temperature 2 wet; RTGP: Real-time Tropospheric Grid Point;
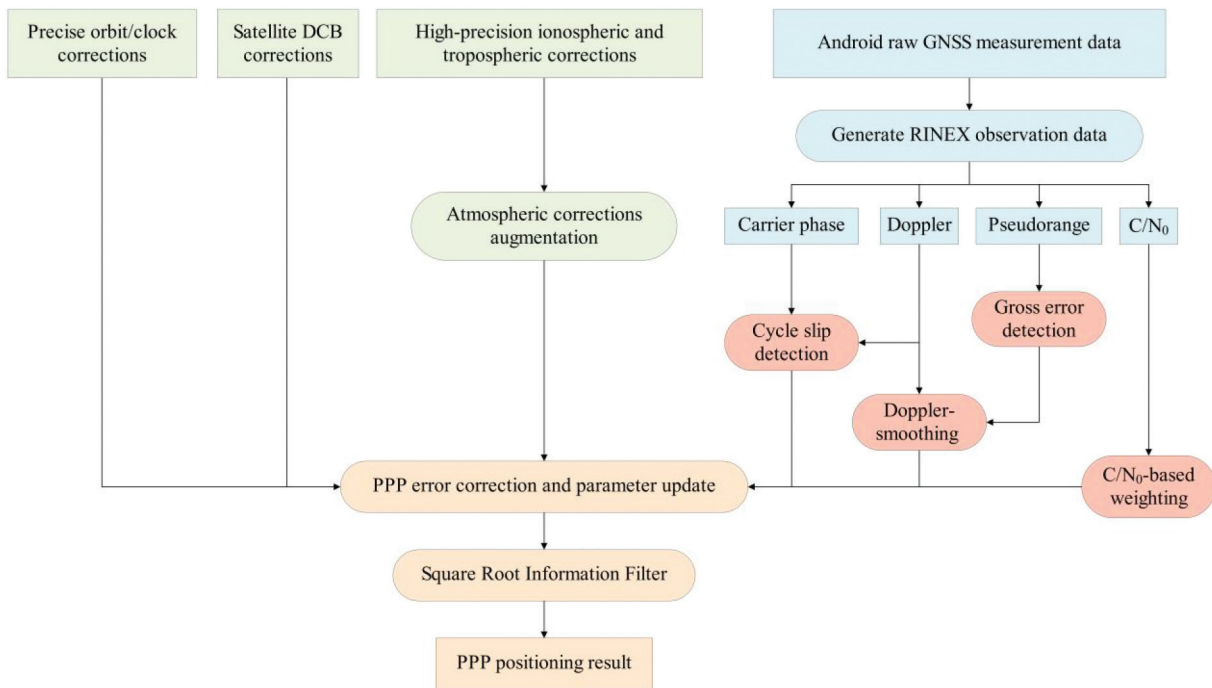TECU: The Total Electron Content

FIGURE 5 Overall flow chart of atmospheric augmentation PPP algorithm. The green color coding represents error correction of space segment and atmosphere segment; the blue color coding represents generation of Android raw GNSS measurement data; the red color coding represents GNSS data preprocessing and weighting strategy; and the yellow color coding represents filtering processing and result.

noise and identify the gross error. Due to the frequent signal loss-of-lock and cycle slips of the carrier phase in smartphone GNSS observations, the Doppler integration method suggested by Zhang et al. (2018) has been developed to detect carrier phase outliers. The carrier-to-noise ratio-based stochastic model proposed in Section 2.3 was adopted to weight GNSS observations; this is because the measurement error of smartphones has a stronger correlation with the carrier-to-noise ratio than with the satellite elevation.

We used International GNSS Service (IGS) precise products to correct satellite-related errors, such as satellite orbit errors, clock errors, and differential code biases (DCBs). For atmospheric delay corrections, we employed the precise ionospheric and tropospheric models established in Section 3.2 to utilize high-precision atmospheric corrections as *a priori* constraints. Because of the lack of information regarding the built-in patch antenna for the receiver-related error corrections, we did not consider the phase center offset (PCO) and phase center variations (PCVs) of the smartphone GNSS antenna. Finally, we linearized the multi-GNSS and dual-frequency PPP observation equations and applied the Square Root Information Filter (SRIF) to estimate the parameters to obtain a more robust positioning result (Dai et al., 2019; PooGyeon & Kailath, 1995).

Table 3 displays the detailed processing strategies used for the atmospheric augmentation PPP and conventional PPP methods for smartphones and Septentrio. The results of a zero-baseline experiment provided in APPENDIX A demonstrated the poor measurement quality of the GLONASS signal tracked by smartphones. Because the observation noise of the GLONASS system is much higher than that of other constellations, we recommend excluding the GLONASS system in the PPP processing. In addition, to eliminate the error caused by the inconsistency of weighting models, the carrier-to-noise ratio (C/N0)-based stochastic model was adopted by both smartphones and the Septentrio receiver in this article. The correlation analysis of the C/N0-based stochastic model and the calibration parameters of all devices is shown in APPENDIX B.

4 | RESULTS

In this section, we present the results of our evaluation of the positioning performance of the atmospheric augmentation PPP and conventional PPP for smartphones and the Septentrio receiver in both static and kinematic positioning. We mainly focused on the convergence speed in the initial stage and positioning accuracy in the horizontal and vertical directions. It should be noted that the only difference between conventional PPP and atmospheric augmentation PPP is the application of different atmospheric corrections.

4.1 | Static Test Analysis

The findings presented in Figure 6 document the number of satellites tracked by different experimental devices in the GPS+BDS+Galileo (G+C+E) combination mode with position dilution of precision (PDOP) at a cut-off angle of 10°. The number of tracking satellites of Huawei P40 in the static environment was 20 to 30, with an average of approximately 24. By contrast, Xiaomi Mi8 tracks a relatively small number of satellites, fluctuating between 16 to 20 with an average of 19 satellites. The Septentrio receiver tracks more satellites (more than 30 on average) and is more stable than smartphones. The PDOP of all the experimental equipment is better than 1.5, indicating that the satellite geometry is ideal under the support of multi-constellation GNSS.

TABLE 3
Detailed Processing Strategies of Atmospheric Augmentation PPP and Conventional PPP Methods for Smartphones and Septentrio in the Same Combined Positioning Mode

Items	Processing strategy
Observations used	Dual-frequency GPS/Galileo (L1/E1+L5/E5a) raw observations Single-frequency BDS (B1I) raw observations
Satellite orbit and clock error	Multi-GNSS orbit and clock products of the GFZ
Satellite differential code bias	MGEX DCB products provided by the CAS
Ionospheric delay error	The Satellite-based Ionospheric Model (SIM) for atmospheric augmentation PPP, while CODE's GIM products for conventional PPP
Tropospheric delay error	ZHD: GPT2w (Böhm et al., 2015) ZWD: The Real-Time Tropospheric Grid Point (RTGP) model for atmospheric augmentation PPP, while the GPT2w model for conventional PPP Mapping function: VMF1 (Boehm et al., 2006)
PCO/PCV	Corrected with igs_14.atx
Earth rotation and relativistic effects	Corrected with the corresponding formula
Receiver clock	Estimated as white noise for each GNSS system
Cut-off angle	10°
Cut-off C/N$_0$	25 dB/Hz for smartphones 30 dB/Hz for Septentrio
Weighting mode	C/N$_0$-based stochastic model
Ambiguity	Estimated as float constant for each continuous arc
Parameters estimation	Square Root Information Filter
Sigma of code	3 m for Mi8, 2 m for P40 and 0.2 m for Septentrio
Sigma of phase	0.008 m for Mi8, 0.006 m for P40 and 0.002 m for Septentrio
Process noises	$10^{-8}\ m^2/s$ for zenith tropospheric delay (Zhang et al., 2020) $0.0016\ m^2/s$ for zenith ionospheric delay (Banville et al., 2014) $20\ m/s$ for the position coordinate state in the kinematic test, while $1\ m/s$ for the position coordinate state in the static test (Naciri & Bisnath, 2021)

The positioning error of the conventional and augmented PPP algorithms employing single-frequency PPP (SF-PPP) and dual-frequency PPP (DF-PPP) solutions was evaluated to determine the effectiveness of the precise atmospheric corrections. The horizontal and vertical positioning errors were calculated as shown in Equation (11):

$$\begin{cases} Horizontal\ error = \sqrt{\delta_N^2 + \delta_E^2} \\ Vertical\ error = \sqrt{\delta_U^2} \end{cases} \tag{11}$$

where δ_N, δ_E, and δ_U represent the error in the east, north, and up directions, respectively, under the station center coordinate system. In addition, we employ the RMS as an index to evaluate the positioning accuracy of PPP in horizontal and vertical directions. The results shown in Figure 7 depict SF-PPP and DF-PPP positioning errors and indicate that the atmospheric augmentation PPP method has
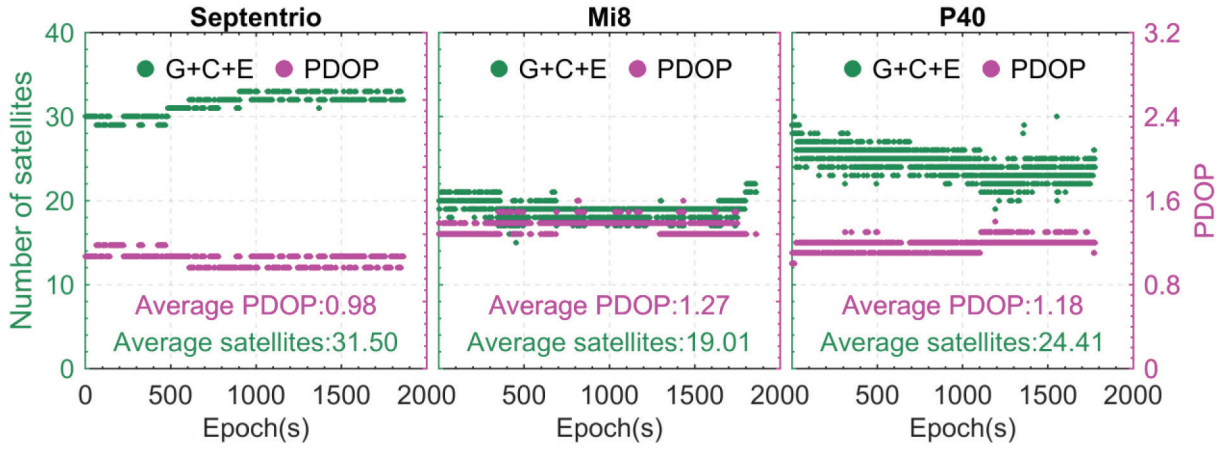
FIGURE 6 PDOP and the number of satellites tracked by each device for the GPS+BDS+Galileo (G+C+E) combination in a static environment
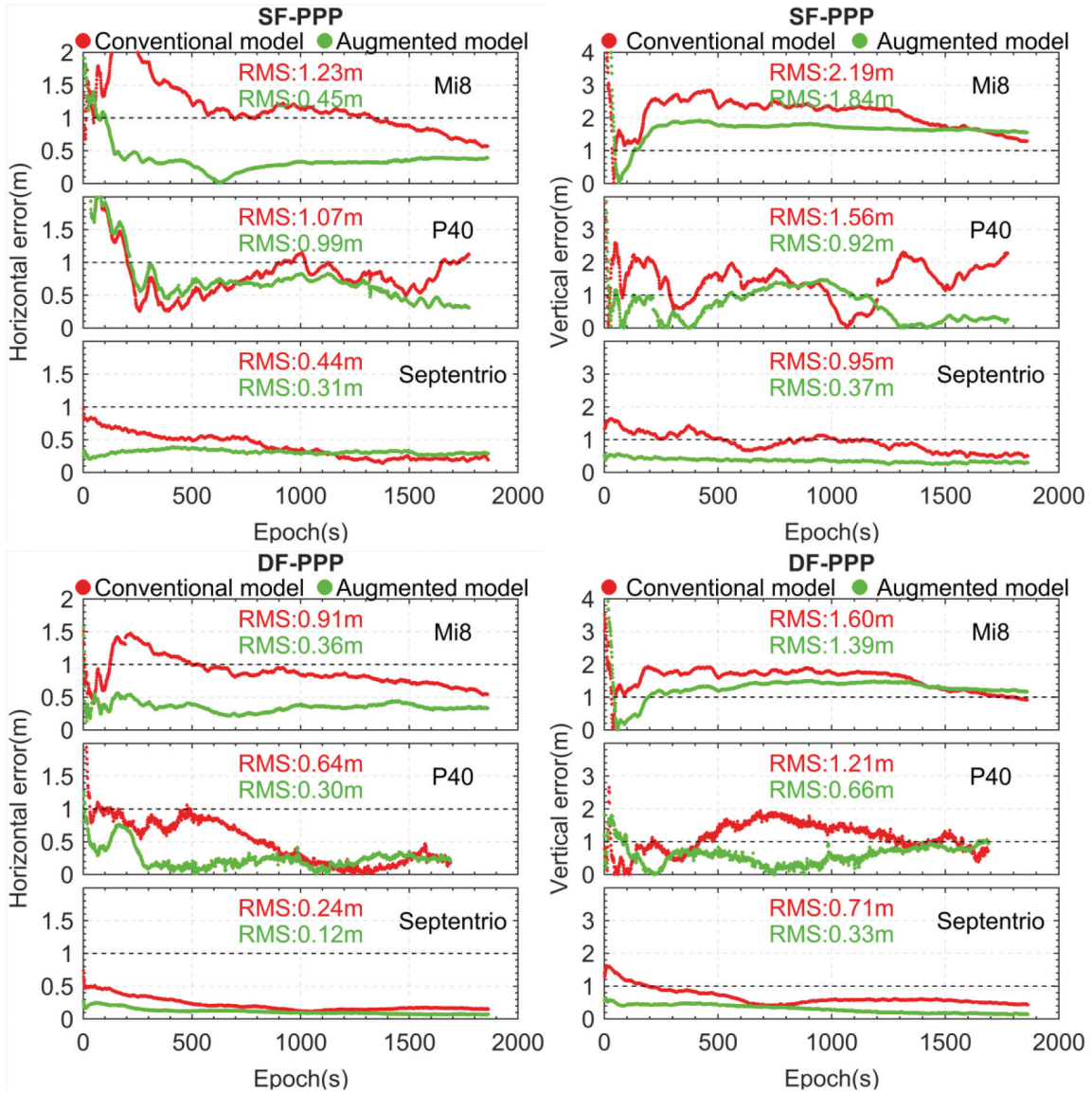

FIGURE 7 Horizontal and vertical positioning errors for different PPP strategies evaluated in a static environment

a significantly improved positioning accuracy and convergence time compared to values obtained using the conventional PPP algorithm. When using the atmospheric augmentation SF-PPP solution, the horizontal positioning errors of the Xiaomi Mi8 and Huawei P40 were 0.45 m and 0.99 m, respectively. Similarly, the vertical positioning errors were 1.84 m and 0.99 m, respectively. The Septentrio receiver achieves positioning accuracy of better than 0.5 m in both the horizontal and vertical directions. Compared with the conventional SF-PPP strategy, the augmented SF-PPP method was effective at improving the positioning performance of both low-cost smartphones and geodetic receivers. In addition, the horizontal positioning accuracy of all the experimental devices was better than 1 m when using the DF-PPP strategy with GPS L5 and Galileo E5a observations. With the help of precise ionospheric and tropospheric corrections, Septentrio and the two smartphones reached positioning accuracy of 0.1 m and 0.3 m in the horizontal direction, respectively. Huawei P40 achieves an accuracy that was better than 1 m, even in the vertical direction; the RMS of the positioning error was 0.66 m. Taken together, our findings revealed that, compared with the conventional DF-PPP model, the atmospheric augmentation DF-PPP model can improve the positioning performance of all experimental devices by more than 50%.

Table 4 displays the horizontal error, vertical error, and convergence time of all three experimental devices using different PPP strategies. For the convergence time in the horizontal direction, we set the threshold value to 1 m $\left(Horizontal\ error < 1\,m \right)$ for the smartphones and 0.5 m $\left(Horizontal\ error < 0.5\,m \right)$ for the Septentrio.

Convergence speed is the most significant obstacle to the consumer application of smartphone PPP technology. To illustrate the benefit of high-precision atmospheric corrections on PPP initialization speed, we determined the time required for different PPP strategies to converge to 1 m in the horizontal direction (the positioning accuracy of successive epochs is better than 1 m). The results shown in Figure 8 document the time comparison of different PPP solutions converging to the horizontal threshold for each experimental device. The DF-PPP strategy leads to a faster convergence speed than the SF-PPP strategy, regardless of whether the precise atmospheric correction is applied. Xiaomi Mi8 and Huawei P40 take about 20 and 30 min, respectively, to converge to within one meter when using the conventional SF-PPP strategy. However, when the atmospheric

TABLE 4
Positioning error and horizontal convergence time for different PPP strategies in the static environment

| PPP strategies (Error unit: meter, time unit: second)		Septentrio mosaic-x5		Xiaomi Mi8		Huawei P40	
		RMS	STD	RMS	STD	RMS	STD
Conventional SF-PPP	Horizontal error	0.44	0.18	1.23	0.39	1.07	0.62
	Vertical error	0.95	0.27	2.18	0.90	1.56	1.55
	Convergence time	762		1331		1774	
Conventional DF-PPP	Horizontal error	0.24	0.10	0.91	0.22	0.64	0.39
	Vertical error	0.71	0.59	1.60	0.59	1.21	0.55
	Convergence time	56		484		530	
Augmented SF-PPP	Horizontal error	0.31	0.03	0.45	0.25	0.99	0.60
	Vertical error	0.36	0.06	1.84	1.11	0.92	0.72
	Convergence time	1		103		214	
Augmented DF-PPP	Horizontal error	0.12	0.04	0.36	0.08	0.30	0.17
	Vertical error	0.33	0.12	1.39	0.79	0.66	0.30
	Convergence time	1		6		4	
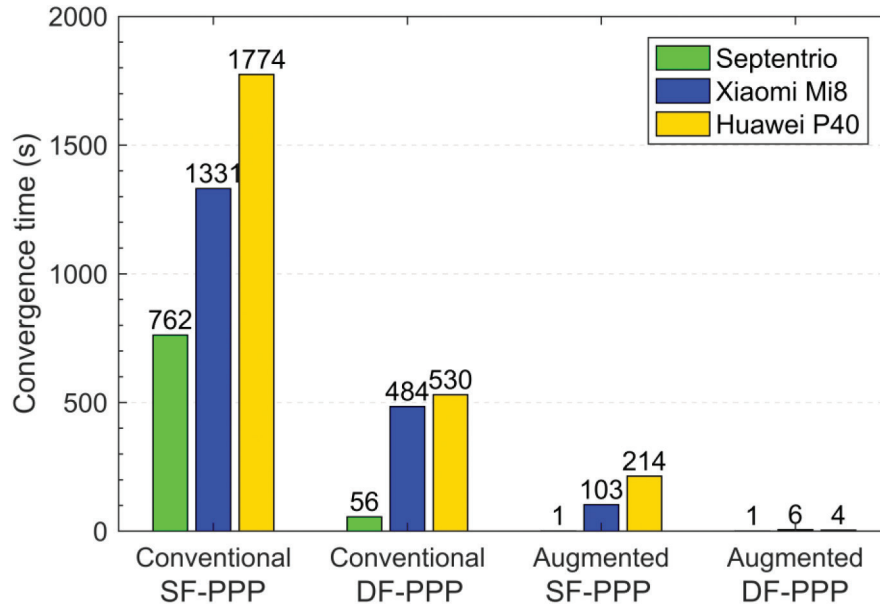
FIGURE 8 Convergence time of horizontal positioning error to the threshold for each experimental device under different PPP strategies in a static environment

augmentation SF-PPP strategy is implemented, the convergence time of the two smartphones is reduced to less than 10 min, with more than a 50% improvement in the convergence speed.

When GPS L5 and Galileo E5a measurements are added, the convergence speed of conventional DF-PPP accelerates dramatically. With these measurements, Xiaomi Mi8 and Huawei P40 achieve a positioning accuracy of better than 1 m in the horizontal direction within 103 s and 214 s, respectively, while Septentrio converges to within 0.5 m in the first epoch. Most remarkably, the Xiaomi Mi8 and Huawei P40 can achieve sub-meter level convergence in seconds (i.e., 6 s and 4 s, respectively) with accurate atmospheric corrections. The results indicate that the multi-constellation and dual-frequency GNSS observations (GPS L1/L5 + Galileo E1/E5a + BDS B1I) augmented by precise regional atmospheric corrections are effective at improving positioning accuracy and can accelerate the PPP convergence speed to achieve sub-meter positioning within 10 s.

It should be noted that it is easy to develop an intuitive misunderstanding that the positioning performance in the kinematic experiment is better than that in the static experiment. The main reason is that there is a sizable and smooth PVC mulch in the static site (as shown in Figure 1) that leads to heavy multipath reflections and affects the positioning performance. While this paper mainly focuses on the performance improvements associated with the use of atmospheric augmentation PPP compared to conventional PPP, we emphasize that one cannot simply compare kinematic and static positioning performance without direct consideration of critical interfering factors in the environment.

4.2 | Kinematic Test Analysis

The findings shown in Figure 9 highlight the kinematic reference trajectories and positioning trajectories of the experimental devices calculated by the atmospheric augmentation DF-PPP algorithm. The kinematic experiment began at
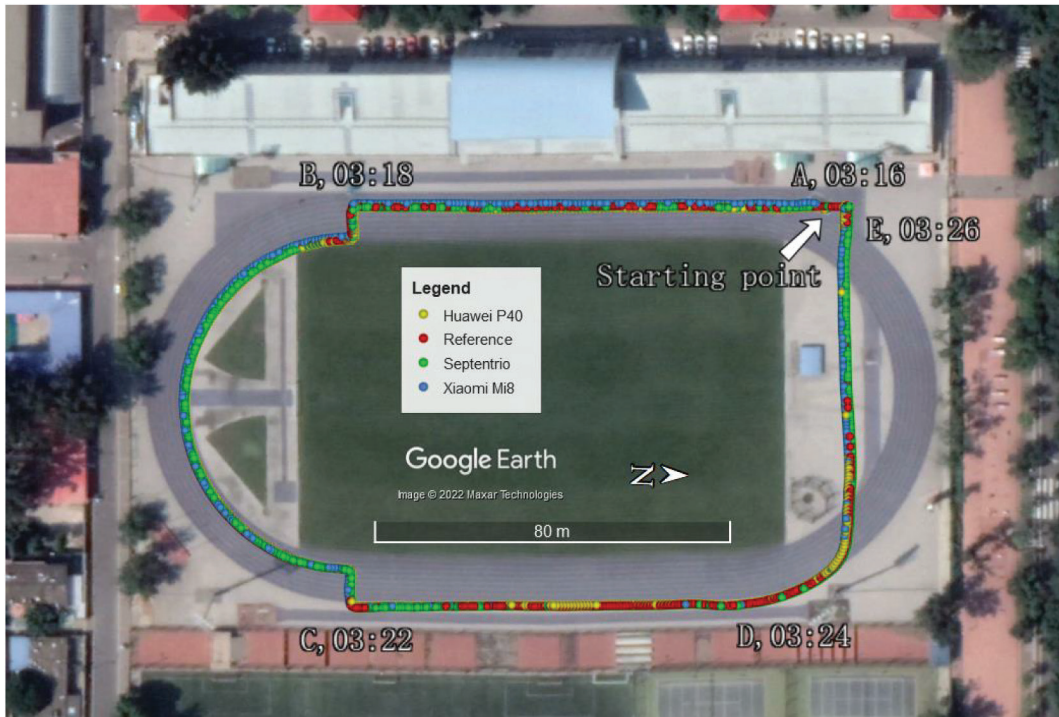
FIGURE 9 Reference and positioning trajectories of each experimental device in the kinematic experiment
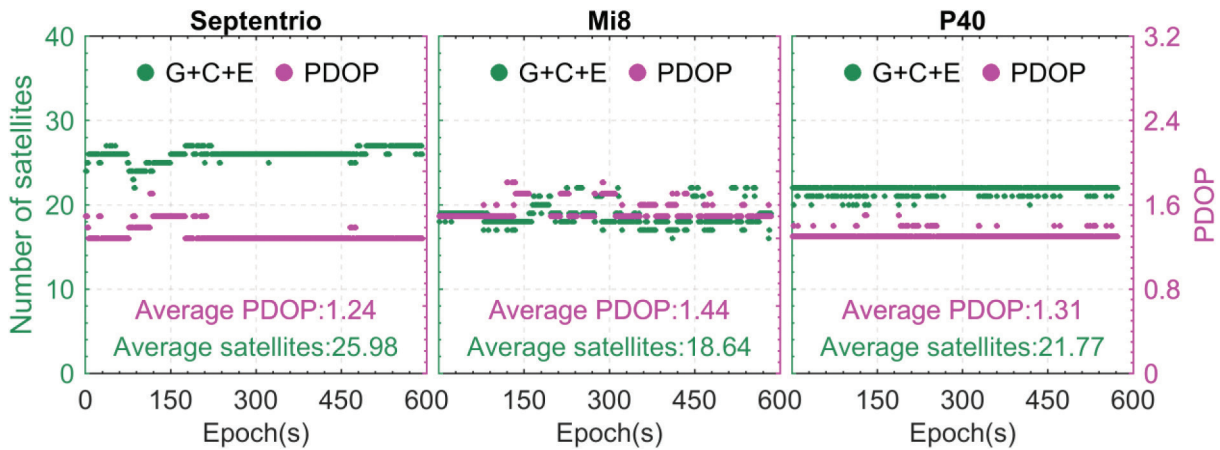All times are displayed in UTC, and the trajectories move anticlockwise from point A to point E.

FIGURE 10 PDOP and the number of satellites tracked by each device for the GPS+BDS+Galileo (G+C+E) combination in the kinematic environment

point A (Starting Point, 03:16). The device was driven for two minutes to corner B (03:18) and then around the circular runway to corner C (03:22). The device was then driven in a straight line to point D (03:22) and turned to reach point E (03:26) to form a closed trajectory.

To compare the satellite tracking capabilities of each experimental device in the kinematic experiment, we determined the number of satellites of GPS+BDS+Galileo (G+C+E) and PDOP with the cut-off angle of 10° as shown in Figure 10. During the experiment, the number of satellites tracked by Xiaomi Mi8 fluctuated between 17 and 23; of note, the PDOP value exceeded 1.8 at one time. With the support of the three satellite systems, approximately 20 satellites were tracked by each device
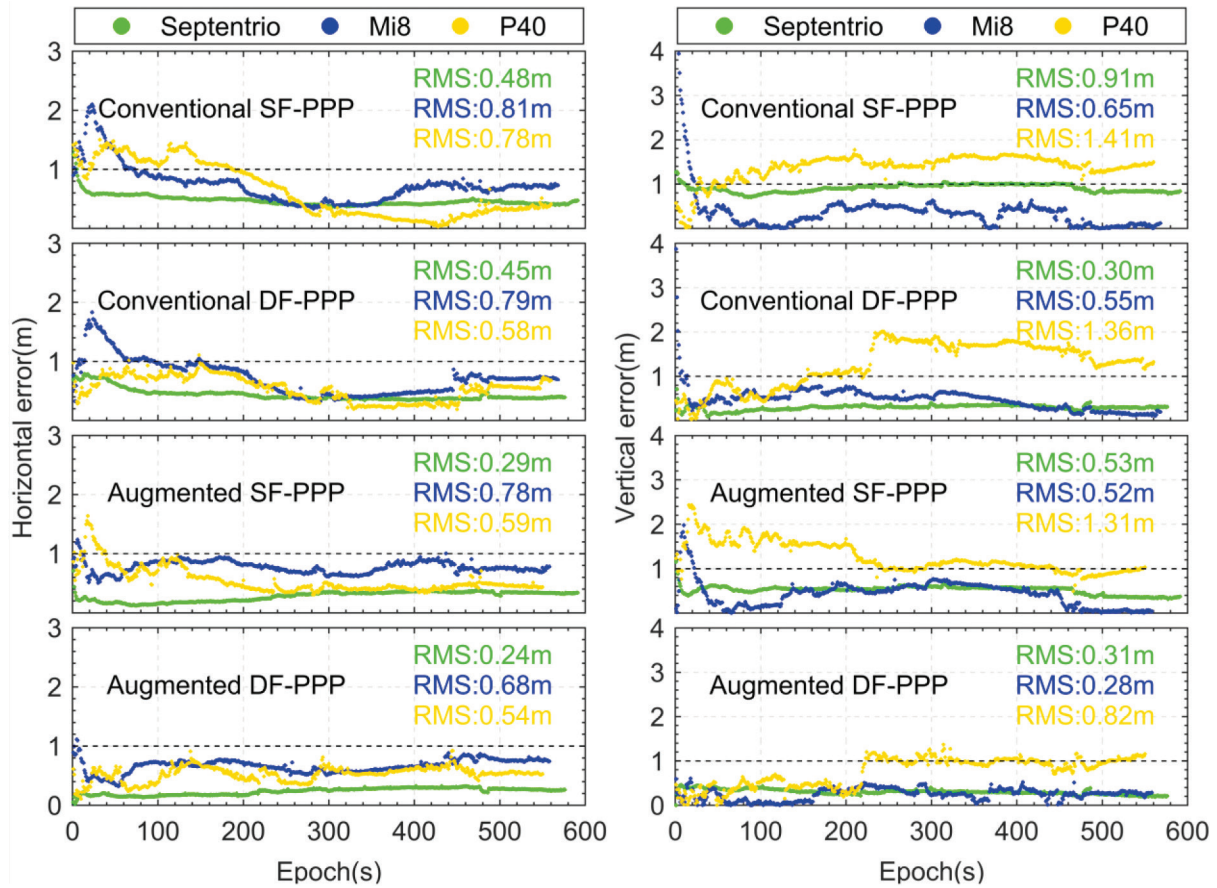
FIGURE 11 Horizontal and vertical positioning error for different PPP strategies evaluated in a kinematic environment

with a PDOP that was better than 2.0; this result indicated that the current satellite geometry is ideal for this application.

The results shown in Figure 11 represent the horizontal and vertical positioning errors of Septentrio, Xiaomi Mi8, and Huawei P40 using the four PPP strategies. The positioning results indicate that the PPP solutions of the three experimental devices can achieve decimeter-level positioning accuracy in the horizontal direction after convergence. At the same time, Xiaomi Mi8 obtains an accuracy of better than 1 m after vertical convergence. As shown in this figure, the atmospheric augmentation PPP technique offers superior horizontal and vertical positioning accuracy compared to the conventional PPP strategy with error sequences that are more stable during the convergence trend. Especially when using the three-constellation DF-PPP method enhanced by high-precision atmospheric corrections, the positioning accuracy of Septentrio, Xiaomi Mi8, and Huawei P40 in the horizontal direction was 0.24 m, 0.68 m, and 0.54 m, respectively. The RMS statistic in the vertical direction was also better than 1 m.

Table 5 documents the horizontal positioning error, vertical positioning error, and the convergence time to the threshold determined for each of the experimental devices in a kinematic environment. Consistent with the static experiment, we set the threshold of convergence time as 1 m $\left(Horizontal\ error < 1\,m \right)$ for smartphones and 0.5 m $\left(Horizontal\ error < 0.5\,m \right)$ for Septentrio.

As in the static experiment, we examined the horizontal convergence speeds of various PPP strategies in a kinematic environment. The results shown in Figure 12 document time comparisons of different PPP solutions that converge

TABLE 5
Positioning Error and Horizontal Convergence Time for Different PPP Strategies in a Kinematic Environment

PPP strategies (Error unit: meter, time unit: second)		Septentrio mosaic-x5		Xiaomi Mi8		Huawei P40	
		RMS	STD	RMS	STD	RMS	STD
Conventional SF-PPP	Horizontal error	0.48	0.10	0.81	0.32	0.78	0.46
	Vertical error	0.91	0.09	0.65	0.53	1.41	0.30
	Convergence time	53		59		167	
Conventional DF-PPP	Horizontal error	0.44	0.10	0.79	0.30	0.59	0.21
	Vertical error	0.30	0.06	0.55	0.27	1.36	0.49
	Convergence time	36		58		148	
Augmented SF-PPP	Horizontal error	0.29	0.09	0.78	0.10	0.59	0.22
	Vertical error	0.53	0.09	0.52	0.30	1.31	0.34
	Convergence time	1		8		32	
Augmented DF-PPP	Horizontal error	0.24	0.06	0.68	0.11	0.54	0.12
	Vertical error	0.31	0.06	0.28	0.13	0.82	0.32
	Convergence time	1		5		1	
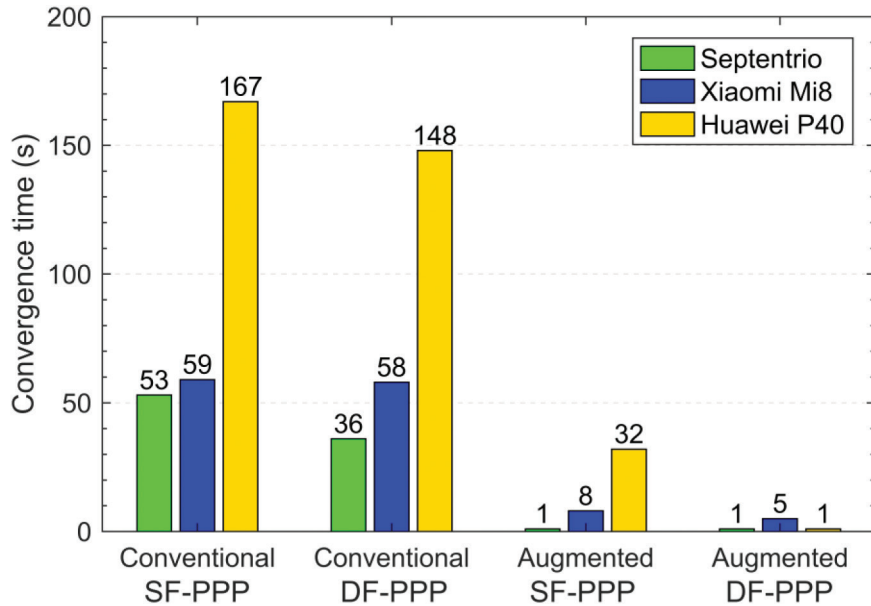
FIGURE 12 Convergence time of horizontal positioning error to the threshold for each experimental device under different PPP strategies in the kinematic environment

to the threshold in the horizontal direction for each experimental device. The statistical positioning results show that convergence to within 1 m in the first epoch is possible for Septentrio, whether one is using SF-PPP or DF-PPP with atmospheric augmentation. For Xiaomi Mi8 and Huawei P40 smartphones, the atmospheric augmentation SF-PPP strategy takes 5 s and 32 s, respectively to converge to 1 m. When using atmospheric augmentation DF-PPP, only 5 s and 1 s, respectively, are needed to converge to the sub-meter level. By contrast, it takes more than 1 to 3 minutes for both smartphones to converge within 1 m when using the conventional PPP model. The kinematic results provide a full demonstration of the effectiveness of the precise regional atmospheric corrections in improving the convergence speed and positioning accuracy for PPP technology.

5 | CONCLUSIONS AND FUTURE WORK

Because of the impact of atmospheric delays and high measurement noise on low-cost smartphones, it is more challenging to attain high-accuracy positioning using the PPP technique; this is especially the case for rapid PPP convergence. This study presents an undifferenced and uncombined PPP method augmented with precise atmospheric corrections to achieve instantaneous sub-meter level positioning of smartphone PPP. Specifically, slant ionospheric delay is established as a Satellite-based Ionospheric Model (SIM) which leads to an RMS accuracy that is better than 1 TECU. The Real-Time Tropospheric Grid Point (RTGP) model has an average accuracy that is better than 1.2 cm. In this study, the performance of the atmospheric augmentation PPP method was evaluated in terms of convergence time, horizontal positioning error, and vertical positioning error.

We first analyzed the stability of the smartphones compared with the Septentrio receiver for tracking the number of satellites and PDOP in an open-sky static experiment. When three constellations (GPS+BDS+Galileo) were applied, approximately 20 satellites were tracked by the two smartphones with an average PDOP value that was better than 1.5. This result revealed that the fusion of multi-GNSS effectively improved the satellites' geometric distribution. According to the positioning results, regardless of the application of precise atmospheric corrections, the convergence speed and positioning error of the DF-PPP solution are superior to those of the SF-PPP solution for each device. When implementing the DF-PPP algorithm that was enhanced with high-quality atmospheric products, Xiaomi Mi8 and Huawei P40 converge to 1 m in the horizontal direction within 6 s and 4 s, respectively; this improves the convergence speed by more than 90% compared with results obtained using the conventional DF-PPP model. For the Septentrio receiver applying SF-PPP and DF-PPP strategies, the atmospheric augmentation solutions can achieve instantaneous horizontal and vertical positioning accuracy that was better than 0.5 m.

Approximately 20 satellites were tracked by smartphones in the kinematic experiment with the PDOP value between 1.2 and 2.0, thus showing lower stability than Septentrio. When using the conventional DF-PPP solution, the horizontal positioning error of the Xiaomi Mi8 and Huawei P40 reached 0.79 m and 0.45 m, respectively. Although the convergence speed is improved compared with SF-PPP, it still takes one and two min for each of the two smartphones to converge to within 1 m. After adopting the atmospheric augmentation PPP strategy presented in this work, all experimental devices achieved sub-meter level positioning accuracy in both horizontal and vertical directions. More importantly, Xiaomi Mi8 and Huawei P40 obtain sub-meter level positioning accuracy within only 5 s and 1 s, respectively. These findings highlight the potential for real-time high-precision application of smartphone PPP.

The undifferenced and uncombined PPP algorithm augmented by high-quality atmospheric corrections closely combines multi-constellation and dual-frequency GNSS measurements with regional atmospheric augmentation technology. We demonstrated that instantaneous sub-meter level convergence is feasible for low-cost smartphones by adopting multi-constellation DF-PPP assisted by atmospheric augmentation. In addition, our studies revealed that ambiguity-fixed positioning solutions may be achieved for smartphones by appropriate calibration and correction of antenna PCO and PCVs (Bochkati et al., 2020; Darugna et al., 2020). Researchers will be able to access the characteristics of the antennae via the GnssAntennaInfo class after Android 11

(API30). This development will motivate further study of high-precision positioning technology for low-cost smartphones (Zangenehnejad & Gao, 2021b). Our future work will focus primarily on achieving fast high-precision positioning in challenging GNSS environments. This will require a combination of atmospheric augmentation PPP technology with multi-source sensors such as MEMS-IMU, magnetometers, and cameras.

ACKNOWLEDGMENTS

REFERENCES

Adjrad, M., Groves, P. D., Quick, J. C., & Ellul, C. (2019). Performance assessment of 3D-mapping-aided GNSS part 2: Environment and mapping. *NAVIGATION, 66*(2), 363–383. http://dx.doi.org/10.1002/navi.289

Banville, S., Collins, P., Zhang, W., & Langley, R. B. (2014). Global and regional ionospheric corrections for faster PPP convergence. *NAVIGATION, 61*(2), 115–124. http://dx.doi.org/10.1002/navi.57

Bochkati, M., Sharma, H., Lichtenberger, C. A., & Pany, T. (2020). Demonstration of fused RTK (fixed) + inertial positioning using Android smartphone sensors only. *Proc. of the IEEE/ION Position, Location and Navigation Symposium (PLANS 2020),* Portland, OR. 1140–1154. https://doi.org/10.1109/PLANS46316.2020.9109865

Boehm, J., Niell, A., Tregoning, P., & Schuh, H. (2006). Global mapping function (GMF): A new empirical mapping function based on numerical weather model data. *Geophysical Research Letters, 33*(7). http://dx.doi.org/10.1029/2005GL025546

Böhm, J., Möller, G., Schindelegger, M., Pain, G., & Weber, R. (2015). Development of an improved empirical model for slant delays in the troposphere (GPT2w). *GPS Solutions, 19*(3), 433–441. http://dx.doi.org/10.1007/s10291-014-0403-7

Brunner, F. K., Hartinger, H., & Troyer, L. (1999). GPS signal diffraction modelling: the stochastic SIGMA-δ model. *Journal of Geodesy, 73*(5), 259–267. http://dx.doi.org/10.1007/s001900050242

Dabove, P., & Di Pietra, V. (2019). Towards high accuracy GNSS real-time positioning with smartphones. *Advances in Space Research, 63*(1), 94–102. http://dx.doi.org/10.1016/j.asr.2018.08.025

Dai, X., Lou, Y., Dai, Z., Qing, Y., Li, M., & Shi, C. (2019). Real-time precise orbit determination for BDS satellites using the square root information filter. *GPS Solutions, 23*(2), 45. http://dx.doi.org/10.1007/s10291-019-0827-1

Darugna, F., Wübbena, J., Ito, A., Wübbena, T., Wübbena, G., & Schmitz, M. (2019). RTK and PPP-RTK using smartphones: From short-baseline to long-baseline applications. *Proc. of the 32nd International Technical Meeting of the Satellite Division of the Institute of Navigation (ION GNSS+ 2019), Miami, FL*. 3932–3945. https://doi.org/10.33012/2019.17078

Darugna, F., Wübbena, J. B., Wübbena, G., Schmitz, M., Schön, S., & Warneke, A. (2020). Impact of robot antenna calibration on dual-frequency smartphone-based high-accuracy positioning: A case study using the Huawei Mate20X. *GPS Solutions, 25*(1). http://dx.doi.org/10.1007/s10291-020-01048-0

Gao, R., Xu, L., Zhang, B., & Liu, T. (2021). Raw GNSS observations from Android smartphones: characteristics and short-baseline RTK positioning performance. *Measurement Science and Technology, 32*(8), 084012. http://dx.doi.org/10.1088/1361-6501/abe56e

Geng, J., Jiang, E., Li, G., Xin, S., & Wei, N. (2019). An improved hatch filter algorithm towards sub-meter positioning using only Android raw GNSS measurements without external augmentation corrections. *Remote Sensing, 11*(14), 1679. http://dx.doi.org/10.3390/rs11141679

Geng, J., & Li, G. (2019). On the feasibility of resolving Android GNSS carrier-phase ambiguities. *Journal of Geodesy, 93*(12), 2621–2635. http://dx.doi.org/10.1007/s00190-019-01323-0

Gong, X., Zheng, F., Gu, S., Zhang, Z., & Lou, Y. (2022). The long-term characteristics of GNSS signal distortion biases and their empirical corrections. *GPS Solutions, 26*(2), 52. http://dx.doi.org/10.1007/s10291-022-01238-y

Gratton, P., Banville, S., Lachapelle, G., & O'Keefe, K. (2021). Kinematic zenith tropospheric delay estimation with GNSS PPP in mountainous areas. *Sensors, 21*(17), 5709. http://dx.doi.org/10.3390/s21175709

Guo, L., Wang, F., Sang, J., Lin, X., Gong, X., & Zhang, W. (2020). Characteristics analysis of raw multi-GNSS measurement from Xiaomi Mi 8 and positioning performance improvement with L5/E5 frequency in an urban environment. *Remote Sensing, 12*(4), 744. http://dx.doi.org/10.3390/rs12040744

Humphreys, T. E., Murrian, M., van Diggelen, F., Podshivalov, S., & Pesyna, K. M. (2016). On the feasibility of cm-accurate positioning via a smartphone's antenna and GNSS chip. *Proc. of the IEEE/ION Position, Location, and Navigation Symposium (PLANS 2016),* Savannah GA. 232–242. http://dx.doi.org/10.1109/PLANS.2016.7479707

Li, G., & Geng, J. (2019). Characteristics of raw multi-GNSS measurement error from Google Android smart devices. *GPS Solutions, 23*(3), 90. http://dx.doi.org/10.1007/s10291-019-0885-4

Li, M., Lei, Z., Li, W., Jiang, K., Huang, T., Zheng, J., & Zhao, Q. (2021). Performance evaluation of single-frequency precise point positioning and its use in the Android smartphone. *Remote Sensing, 13*(23), 4894. http://dx.doi.org/10.3390/rs13234894

Li, W., Zhu, X., Chen, Z., Dai, Z., Li, J., & Ran, C. (2021). Code multipath error extraction based on the wavelet and empirical mode decomposition for Android smart devices. *GPS Solutions, 25*(3), 91. http://dx.doi.org/10.1007/s10291-021-01122-1

Li, X., Li, X., Yuan, Y., Zhang, K., Zhang, X., & Wickert, J. (2018). Multi-GNSS phase delay estimation and PPP ambiguity resolution: GPS, BDS, GLONASS, Galileo. *Journal of Geodesy, 92*(6), 579–608. http://dx.doi.org/10.1007/s00190-017-1081-3

Liu, F., Elsheikh, M., Gao, Y., & El-Sheimy, N. (2021). Fast Convergence Real-Time Precise Point Positioning with Android Smartphone GNSS Data. *Proc. of the 34th International Technical Meeting of the Satellite Division of the Institute of Navigation (ION GNSS+ 2021),* St. Louis, MO. 3049–3058. http://dx.doi.org/10.33012/2021.18052

Liu, Q., Gao, C., Peng, Z., Zhang, R., & Shang, R. (2021). Smartphone positioning and accuracy analysis based on real-time regional ionospheric correction model. *Sensors, 21*(11), 3879. http://dx.doi.org/10.3390/s21113879

Liu, T., Zhang, B., Yuan, Y., & Li, M. (2018). Real-time precise point positioning (RTPPP) with raw observations and its application in real-time regional ionospheric VTEC modeling. *Journal of Geodesy, 92*(11), 1267–1283. http://dx.doi.org/10.1007/s00190-018-1118-2

Liu, W., Shi, X., Zhu, F., Tao, X., & Wang, F. (2019). Quality analysis of multi-GNSS raw observations and a velocity-aided positioning approach based on smartphones. *Advances in Space Research, 63*(8), 2358–2377. http://dx.doi.org/10.1016/j.asr.2019.01.004

Magalhães, A., Bastos, L., Maia, D., & Gonçalves, J. A. (2021). Relative positioning in remote areas using a GNSS dual frequency smartphone. *Sensors, 21*(24), 8354. http://dx.doi.org/10.3390/s21248354

Naciri, N., & Bisnath, S. (2021). An uncombined triple-frequency user implementation of the decoupled clock model for PPP-AR. *Journal of Geodesy, 95*(5), 60. http://dx.doi.org/10.1007/s00190-021-01510-y

Ng, H.-F., Zhang, G., Luo, Y., & Hsu, L.-T. (2021). Urban positioning: 3D mapping-aided GNSS using dual-frequency pseudorange measurements from smartphones. *NAVIGATION, 68*(4), 727–749. http://dx.doi.org/10.1002/navi.448

Paziewski, J., Fortunato, M., Mazzoni, A., & Odolinski, R. (2021). An analysis of multi-GNSS observations tracked by recent Android smartphones and smartphone-only relative positioning results. *Measurement, 175*. http://dx.doi.org/10.1016/j.measurement.2021.109162

Paziewski, J., Sieradzki, R., & Baryla, R. (2019). Signal characterization and assessment of code GNSS positioning with low-power consumption smartphones. *GPS Solutions, 23*(4), 98. http://dx.doi.org/10.1007/s10291-019-0892-5

PooGyeon, P., & Kailath, T. (1995). New square-root algorithms for Kalman filtering. *IEEE Transactions on Automatic Control, 40*(5), 895–899. http://dx.doi.org/10.1109/9.384225

Robustelli, U., Paziewski, J., & Pugliano, G. (2021). Observation quality assessment and performance of GNSS standalone positioning with code pseudoranges of dual-frequency Android smartphones. *Sensors, 21*(6), 2125. http://dx.doi.org/10.3390/s21062125

Shinghal, G., & Bisnath, S. (2021). Conditioning and PPP processing of smartphone GNSS measurements in realistic environments. *Satellite Navigation, 2*(1), 10. http://dx.doi.org/10.1186/s43020-021-00042-2

Wang, G., Bo, Y., Yu, Q., Li, M., Yin, Z., & Chen, Y. (2020). Ionosphere-constrained single-frequency PPP with an Android smartphone and assessment of GNSS observations. *Sensors, 20*(20), 5917. http://dx.doi.org/10.3390/s20205917

Wang, L., Li, Z., Wang, N., & Wang, Z. (2021). Real-time GNSS precise point positioning for low-cost smart devices. *GPS Solutions, 25*(2), 69. http://dx.doi.org/10.1007/s10291-021-01106-1

Wang, Z., Xue, K., Wang, C., Zhang, T., Fan, L., Hu, Z., Shi, C., Jing, G. (2021). Near real-time modeling of global ionospheric vertical total electron content using hourly IGS data. *Chinese Journal of Aeronautics, 34*(2), 386–395. http://dx.doi.org/10.1016/j.cja.2020.07.023

Wanninger, L., & Heßelbarth, A. (2020). GNSS code and carrier phase observations of a Huawei P30 smartphone: quality assessment and centimeter-accurate positioning. *GPS Solutions, 24*(2), 64. http://dx.doi.org/10.1007/s10291-020-00978-z

Wieser, A., & Brunner, F. K. (2000). An extended weight model for GPS phase observations. *Earth, Planets and Space, 52*(10), 777–782. http://dx.doi.org/10.1186/BF03352281

Wu, Q., Sun, M., Zhou, C., & Zhang, P. (2019). Precise point positioning using dual-frequency GNSS observations on smartphone. *Sensors, 19*(9), 2189. http://dx.doi.org/10.3390/s19092189

Xia, Y., Meng, X., Yang, Y., Pan, S., Zhao, Q., & Gao, W. (2021). First results of BDS positioning for LBS applications in the UK. *Satellite Navigation, 2*(1), 8. http://dx.doi.org/10.1186/s43020-021-00035-1

Yi, D., Bisnath, S., Naciri, N., & Vana, S. (2021). Effects of ionospheric constraints in precise point positioning processing of geodetic, low-cost and smartphone GNSS measurements. *Measurement, 183*, 109887. http://dx.doi.org/10.1016/j.measurement.2021.109887

Yong, C. Z., Odolinski, R., Zaminpardaz, S., Moore, M., Rubinov, E., Er, J., & Denham, M. (2021). Instantaneous, dual-frequency, multi-GNSS precise RTK positioning using Google Pixel 4 and Samsung Galaxy S20 Smartphones for zero and short baselines. *Sensors, 21*(24), 8318. http://dx.doi.org/10.3390/s21248318

Yuan, H., Zhang, Z., He, X., Li, G., & Wang, S. (2022). Stochastic model assessment of low-cost devices considering the impacts of multipath effects and atmospheric delays. *Measurement, 188*, 110619. http://dx.doi.org/10.1016/j.measurement.2021.110619

Zangenehnejad, F., & Gao, Y. (2021a). Application of U of C model based multi-GNSS PPP to smartphones GNSS positioning. *Proc. of the 34th International Technical Meeting of the Satellite Division of the Institute of Navigation (ION GNSS+ 2021),* St. Louis, MO. 2986–3003. http://dx.doi.org/10.33012/2021.18123

Zangenehnejad, F., & Gao, Y. (2021b). GNSS smartphones positioning: advances, challenges, opportunities, and future perspectives. *Satellite Navigation, 2*(1), 24. https://doi.org/10.1186/s43020-021-00054-y

Zeng, S., Kuang, C., & Yu, W. (2022). Evaluation of real-time kinematic positioning and deformation monitoring using Xiaomi Mi 8 smartphone. *Applied Sciences, 12*(1) 435. http://dx.doi.org/10.3390/app12010435

Zhang, K., Jiao, W., Wang, L., Li, Z., Li, J., & Zhou, K. (2019). Smart-RTK: Multi-GNSS kinematic positioning approach on Android smart devices with Doppler-smoothed-code filter and constant acceleration model. *Advances in Space Research, 64*(9), 1662–1674. http://dx.doi.org/10.1016/j.asr.2019.07.043

Zhang, X., Li, P., Tu, R., Lu, X., Ge, M., & Schuh, H. (2020). Automatic calibration of process noise matrix and measurement noise covariance for multi-GNSS precise point positioning. *Mathematics, 8*(4), 502. http://dx.doi.org/10.3390/math8040502

Zhang, X., Tao, X., Zhu, F., Shi, X., & Wang, F. (2018). Quality assessment of GNSS observations from an Android N smartphone and positioning performance analysis using time-differenced filtering approach. *GPS Solutions, 22*(3), 70. http://dx.doi.org/10.1007/s10291-018-0736-8

Zhao, Q., Yao, Y., Yao, W., & Li, Z. (2018). Real-time precise point positioning-based zenith tropospheric delay for precipitation forecasting. *Scientific Reports, 8*(1) 7939. http://dx.doi.org/10.1038/s41598-018-26299-3

Zheng, F., Gu, S., Gong, X., Lou, Y., Fan, L., & Shi, C. (2019). Real-time single-frequency pseudorange positioning in China based on regional satellite clock and ionospheric models. *GPS Solutions, 24*(1), 6. http://dx.doi.org/10.1007/s10291-019-0923-2

Zheng, F., Lou, Y., Gu, S., Gong, X., & Shi, C. (2018). Modeling tropospheric wet delays with national GNSS reference network in China for BeiDou precise point positioning. *Journal of Geodesy, 92*(5), 545–560. http://dx.doi.org/10.1007/s00190-017-1080-4

APPENDIX A: GNSS OBSERVATION NOISE ANALYSIS

Multi-constellation GNSS can increase the number of visible satellites and improve the geometric distribution of the satellites to obtain better positioning accuracy and reliability. However, one prerequisite for improving positioning quality using multi-constellation GNSS is that each constellation must have consistent

and high-precision ranging accuracy. We stated in Section 3.3 that only GPS/BDS/ Galileo systems were used for PPP processing and that the GLONASS system was excluded. This was because GLONASS observation errors were much larger than those of other constellations.

Zero-baseline double-difference (DD) eliminates orbital errors, satellite/receiver clock errors, and atmospheric delays. DD residuals can be used to evaluate the measurement accuracy/observation noise of GNSS receivers (Humphreys et al., 2016). We conducted a zero-baseline experiment to obtain an objective comparison of each constellation's code observation noise. In addition to the Xiaomi Mi8, Huawei P40, and Septentrio mosaic-X5 featured in the paper, we also added receivers from other brands for comparison, including the Samsung S20, Xiaomi Mi11 Smartphone, and the low-cost Ublox F9P. The schematic and physical diagram of the zero-baseline experiment are shown in Figure 13:

The RF shield box and Multi-GNSS Choke Ring Antenna can effectively absorb multipath reflections. Thus, we can assume that the zero-baseline DD residuals represent nearly pure observation noise of the GNSS chip inside the smartphones. The experiment lasted about 11 hours, from 1:56 to 13:16 UTC. We calculated the standard deviation (STD) of the observation noise for six constellations and dual-frequency code observations (separately for BDS-2 and BDS-3):

As shown, only the geodetic Septentrio mosaic-X5 exhibited a consistent accuracy of around 0.2 m for all constellations and frequencies. However, all smartphones and the low-cost U-blox F9P have a large observation noise with GLONASS that is more than three to four times higher than those resulting from the other constellations. The GLONASS observation noise of Xiaomi Mi8 and Huawei P40 is up to about four meters; with Samsung S20 and Xiaomi 11, the observation noise can be as high as eight meters.

Figure 15 depicts the time series of the code observation noise for 11 hours in the zero-baseline experiment. It should be noted that the maximum value in the range of the vertical coordinates of the GLONASS system shown in this figure is 40
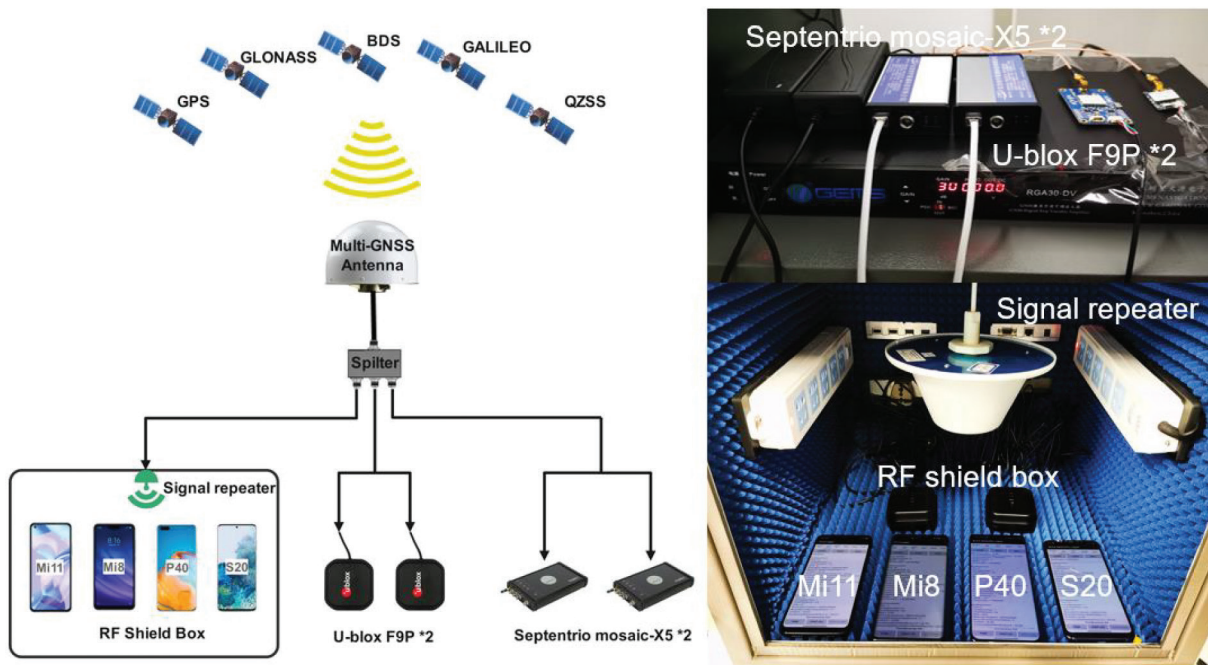

FIGURE 13 Schematic and physical diagram of the zero-baseline experiment for evaluating GNSS observation noise
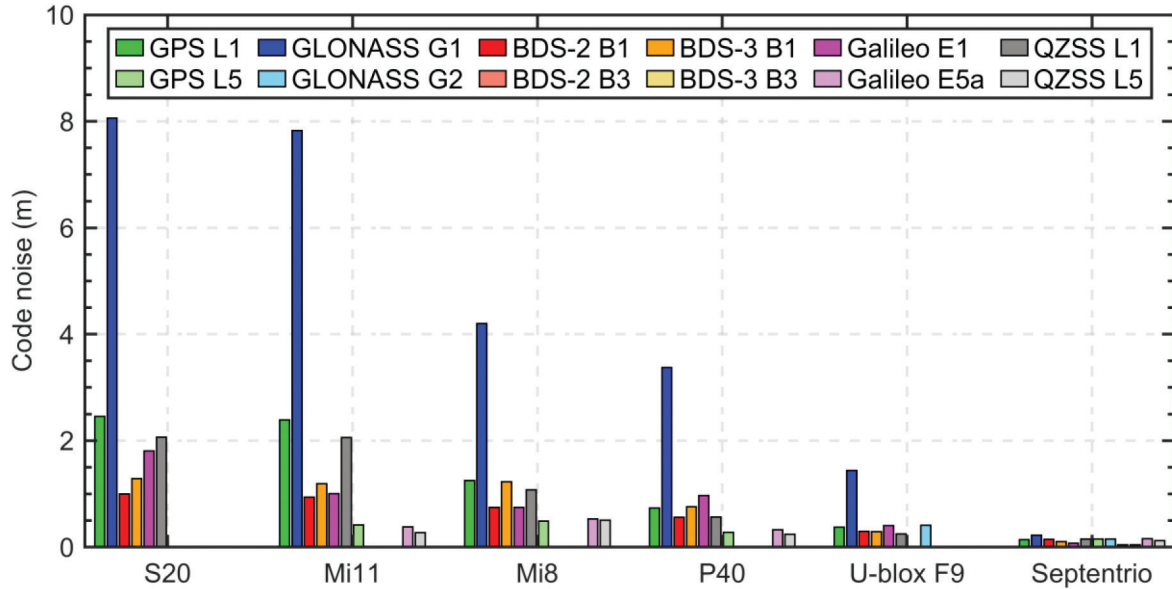
FIGURE 14 Root-mean-square error of code observation noise of different GNSS devices in zero-base line experiment.

m; the maximum value of the other vertical coordinates is 20 m. The observation noise of the GLONASS system for four smartphones is up to approximately 30 m, which is much higher than that reported for the other constellations. The results reveal that adding the GLONASS system to the GNSS positioning algorithm will not improve the positioning accuracy when the visible satellites are sufficient. On the contrary, the addition of GLONASS will be deleterious if one hopes to use the smartphone/low-cost receiver to achieve high-precision positioning.

Similar experimental conclusions were reported by Zangenehnejad and Gao (2021a) and Xia et al. (2021). Therefore, we recommend omitting the GLONASS system when there are more than four visible satellites to avoid deterioration of the positioning performance for low-cost smartphones and receivers. As for the QZSS system, the smartphone could only track one or two satellites in our experiments and received no signals during most of the observation time. Therefore, we noted in Table 3 that only GPS/BDS/Galileo raw observations were used, despite the fact that smartphones are ostensibly capable of supporting both GLONASS and QZSS.

APPENDIX B: COEFFICIENTS CALIBRATION OF STOCHASTIC MODEL

The carrier-to-noise ratio is an important factor in measuring the signal quality of GNSS receivers. A higher carrier-to-noise ratio represents better measurement quality and signal tracking. Existing studies have proved that the C/N_0-based weighting scheme is more suitable than the elevation-based model for smart-phones with built-in linearly polarized microstrip antennae (Zangenehnejad & Gao, 2021b). We presented an improved C/N_0-based weighting model in Section 2.3.1. To determine the stochastic model coefficients for each device, we used the short-baseline single-difference (SD) method proposed by Zhang et al. (2018) to extract the code residuals. The findings shown in Figure 16 document the correlation between the SD residuals and C/N_0/elevation of the Huawei P40 and Septentrio mosaic-X5.
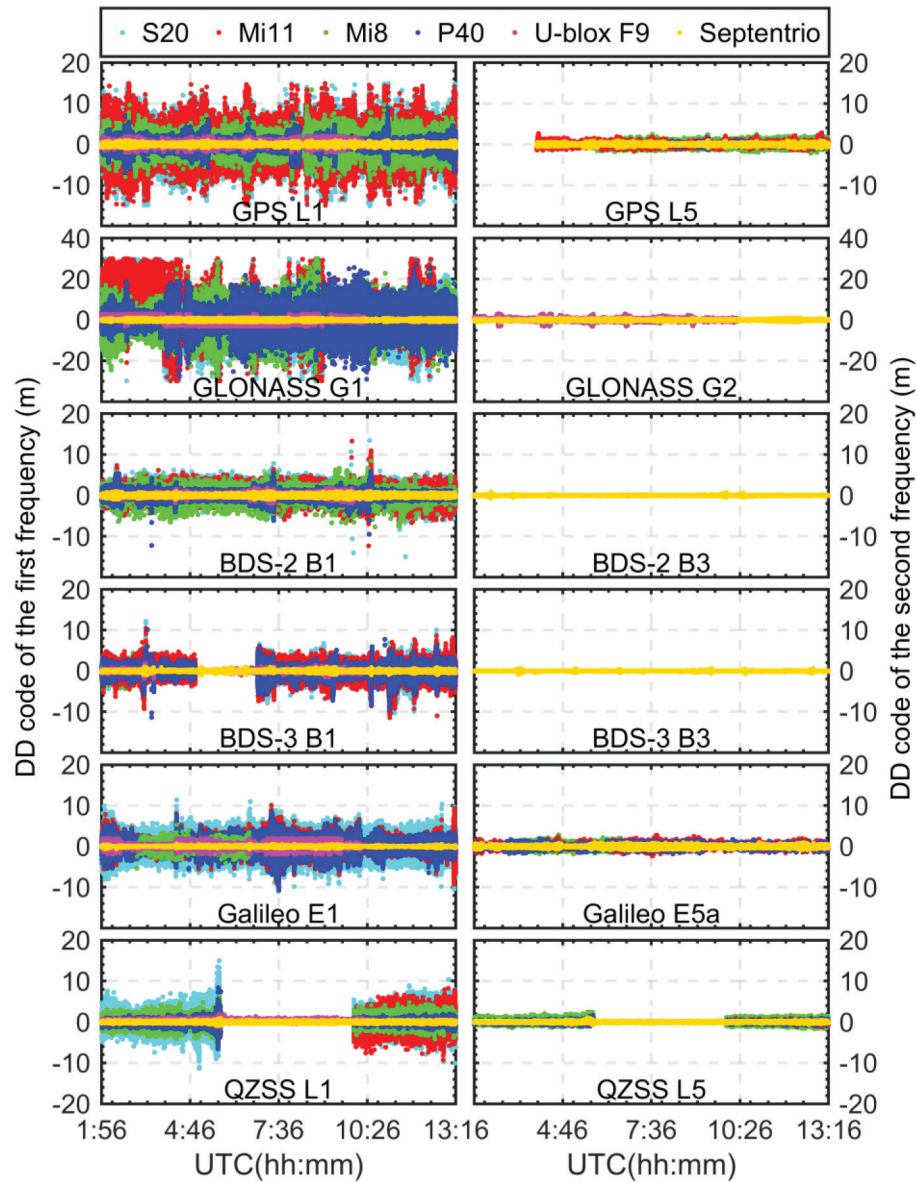
FIGURE 15 Time series of the code observation noise for different GNSS devices used in the zero baseline experiment.
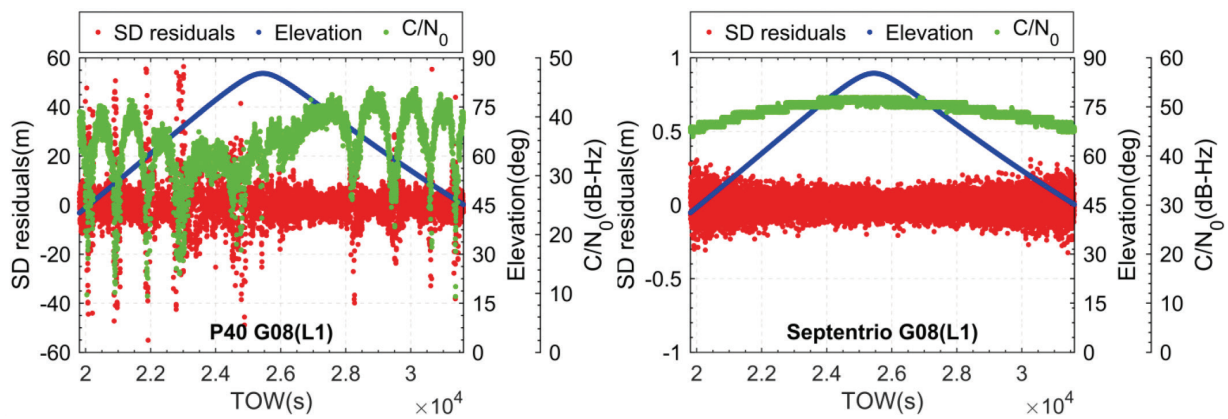

FIGURE 16 Correlation of code SD residuals with C/N_0 and elevation for GPS G08
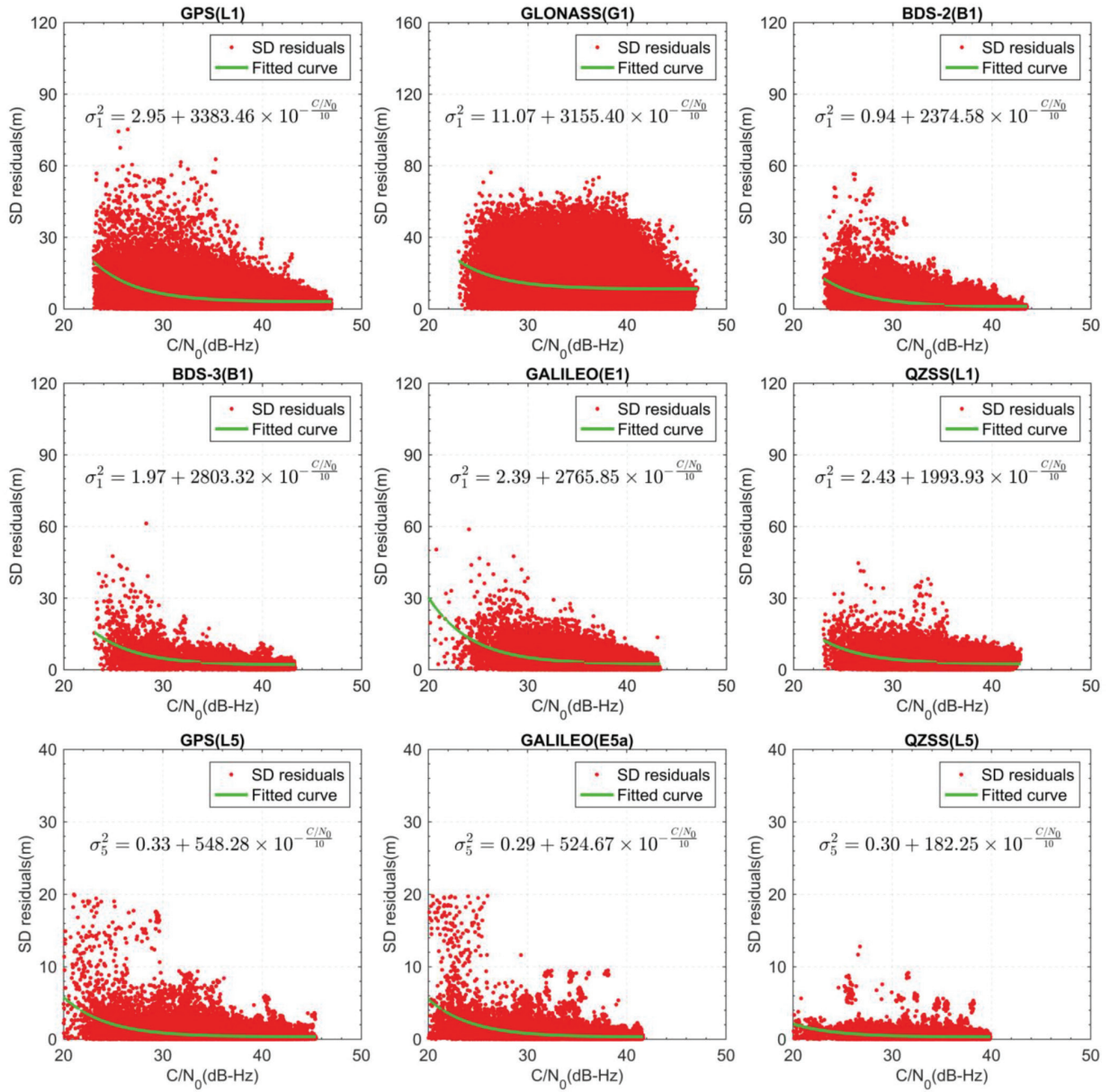The Huawei P40 smartphone is shown on the left and the Septentrio mosaic-X5 receiver is shown on the right.

FIGURE 17 Stochastic model coefficients obtained by fitting SD residuals and C/N$_0$ for the Xiaomi Mi8 smartphone
The first two rows present the code SD residuals and fitted curves of the first frequency. The final row presents the code SD residuals and fitted curves of the second frequency.

The short-baseline inter-station single-difference (SD) residuals of code observations are mainly the effect of multipath and noise, which are properties that reflect the GNSS measurement quality in the natural environment (Zhang et al., 2018). The measurement quality of the P40 smartphone correlates only with the C/N$_0$, while the measurement quality of the Septentrio mosaic-X5 receiver maintains good correlations with both C/N$_0$ and elevation. To unify the stochastic model, data from both smartphones and the Septentrio receiver were analyzed using Equation (9) to weigh the GNSS observations. Table 6 provides the fitted coefficients of the C/N$_0$-based stochastic model for all devices.

Figures 17 to 19 document the stochastic model curves of Xiaomi Mi8, Huawei P40, and Septentrio mosaic-X5 obtained by fitting the code SD residuals and C/N$_0$. The coefficients of these stochastic models need to be calibrated only once and can

TABLE 6

Fitted Coefficients of the C/N0-Based Stochastic Model for Each Constellation and Frequency of Xiaomi Mi8, Huawei P40, and Septentrio mosaic-X5

| Constellation and frequency		Xiaomi Mi8		Huawei P40		Septentrio mosaic-x5	
		V	C	V	C	V	C
GPS	L1	2.95	3383.46	3.21	515.57	0.13	1097.16
	L5	0.33	548.28	0.73	119.31	0.06	532.46
GLONASS	G1	11.07	3155.40	6.74	1082.70	0.27	2728.96
BDS-2	B1I	0.94	2374.58	2.62	317.77	0.19	359.52
BDS-3	B1I	1.97	2803.32	3.87	371.72	0.16	1131.91
Galileo	E1	2.39	2765.85	3.74	317.32	0.11	595.05
	E5a	0.29	524.67	0.61	106.33	0.06	275.60
QZSS	L1	2.43	1993.93	1.02	2207.67	0.10	425.92
	L5	0.30	182.25	0.46	73.01	0.05	184.90
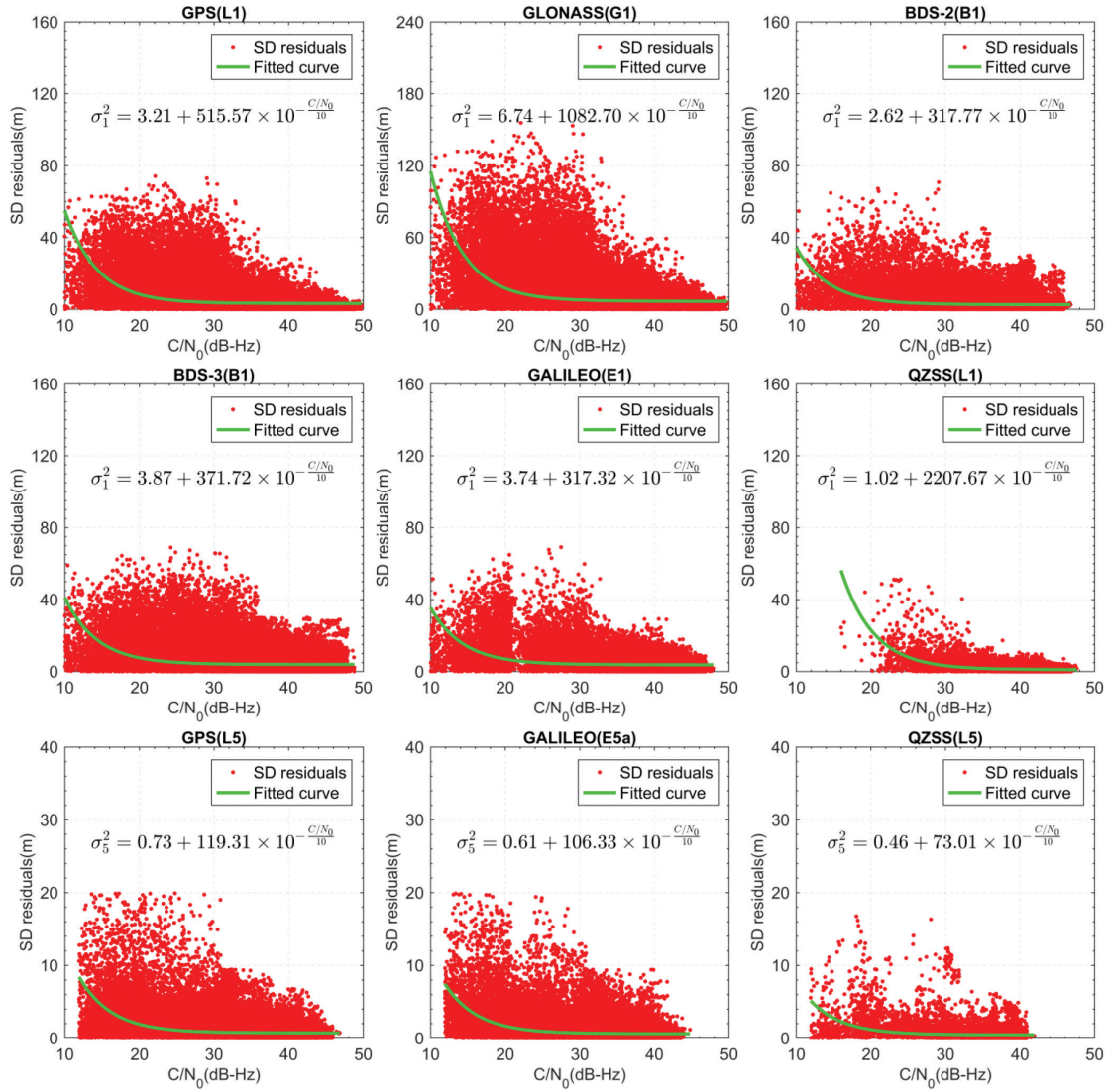
FIGURE 18 Stochastic model coefficients obtained by fitting SD residuals and C/N$_0$ for the Huawei P40 smartphone

The first two rows present the code SD residuals and fitted curves of the first frequency. The final row presents the code SD residuals and fitted curves of the second frequency.
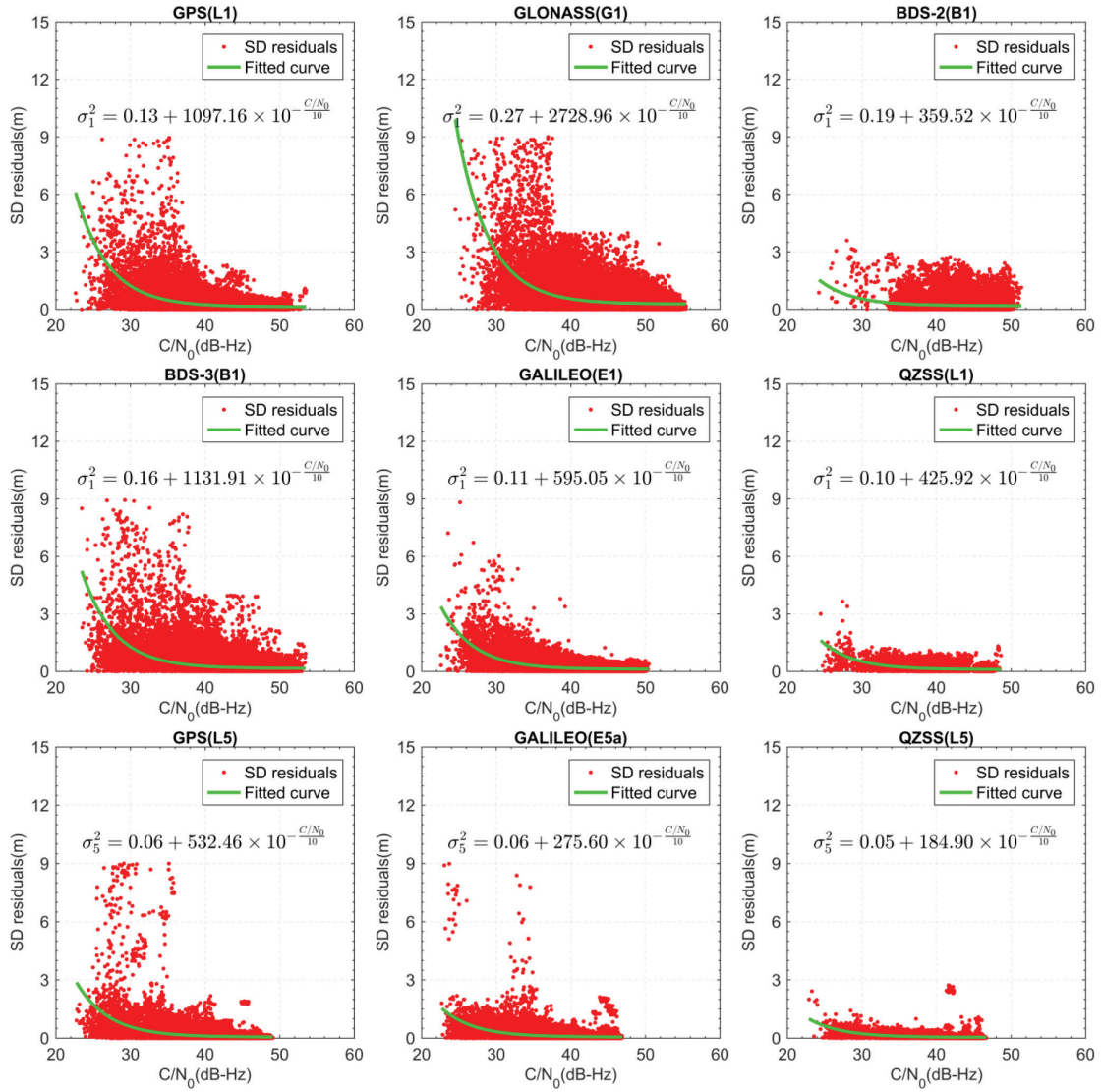
FIGURE 19 Stochastic model coefficients obtained by fitting SD residuals and C/N$_0$ for the Septentrio mosaic-X5 receiver The first two rows present the code SD residuals and fitted curves of the first frequency. The final row presents the code SD residuals and fitted curves of the second frequency.

be applied in other environments as an *a priori* weighting function. We calibrated the stochastic model coefficients at the first frequency for all constellations, including GPS L1, GLONASS G1, BDS-2 B1I, BDS-3 B1I, Galileo E1, and QZSS L1. We also calibrated the coefficients of GPS L5, Galileo E5a, and QZSS L5 on the second frequency.